Poro-viscoelastic tidal heating of Io

Hay, Hamish C. F. C.; Hewitt , Ian; Rovira Navarro, M.; Katz, Richard F.

DOI
10.1098/rspa.2025.0607

Publication date
2025

Document Version
Final published version

Published in
Royal Society of London. Proceedings A. Mathematical, Physical and Engineering Sciences

PROCEEDINGS A

royalsocietypublishing.org/journal/rspa

Research

Cite this article: Hay HCFC, Hewitt I, Rovira-Navarro M, Katz RF. 2025 Poro-viscoelastic tidal heating of Io. *Proc. R. Soc. A* **481**: 20250607. https://doi.org/10.1098/rspa.2025.0607

Received: 11 July 2025
Accepted: 19 September 2025

Subject Areas:
solar system, geophysics, applied mathematics

Keywords:
poroelasticity, viscous compaction, tides, tidal heating, magmatism

Author for correspondence:
Hamish C. F. C. Hay
e-mail: hcfch1@st-andrews.ac.uk

Poro-viscoelastic tidal heating of Io

Hamish C. F. C. Hay[1,†], Ian Hewitt[2], Marc Rovira-Navarro[3] and Richard F. Katz[1]

[1]Department of Earth Sciences, and [2]Mathematical Institute, University of Oxford, Oxford, UK
[3]Faculty of Aerospace Engineering, TU Delft, Delft, The Netherlands

HCFCH, 0000-0003-1746-1228; IH, 0000-0002-9167-6481; RFK, 0000-0001-8746-5430

Io's tidally driven global volcanism indicates widespread partial melting in its mantle. How this melt participates in the interior dynamics and, in particular, the role it plays in tidal dissipation, is poorly understood. We model Io's tidal deformation by treating its mantle as a two-phase (solid and melt) system. By combining poro-viscous and poro-elastic compaction theories in a Maxwell framework with a consistent model of tidal and self-gravitation, we produce the first self-consistent evaluation of Io's tidal heating rate due to shearing, compaction and Darcy flow. We find that Darcy dissipation can potentially exceed shear heating, but only for large (0.05–0.2) melt fractions, and if the grain size is large or melt viscosity ultra-low. Since grain sizes larger than 1 cm are unlikely, this suggests that Darcy dissipation is secondary to shear dissipation. Compaction dissipation is maximized when the asthenosphere is highly resistive to isotropic stresses, but contributes at most 1% of Io's observed heating rate. This work represents a crucial step toward a self-consistent quantitative theory for the dynamics of Io's partially molten interior.

1. Introduction

Io, the innermost Galilean moon of Jupiter, is the most volcanically active body in our solar system [1], with a thermal output of approximately 100 TW [2], roughly 10^5 times that of Earth's similarly sized moon [3]. Io's volcanism is powered by tides, which transfer orbital energy to the interior via Jupiter's gravitational field

†Present address: School of Mathematics and Statistics, University of St Andrews, St Andrews, UK.

Electronic supplementary material is available online at https://doi.org/10.6084/m9.figshare.c.8061268.

THE ROYAL SOCIETY PUBLISHING

[4]. These tides are the result of viscoelastic deformation in its interior, dissipating heat that drives melting. The buoyant melt segregates from the residual solid, accumulating at the near-surface before either refreezing or erupting [5]. As melt segregates, the residual solid compacts [6]. A physically consistent description of Io's internal dynamics must therefore combine tidal deformation, melt segregation, compaction and viscous dissipation into a single theory describing the two-phase dynamics of partially molten rock. Here we take a first step towards this theory.

Io's volcanism has been observed for decades with passing spacecraft [7–10] and ground-based telescopes [11–16]. The texture and internal location of the erupted magma's reservoir has remained elusive. The detection of an anomalous, induced magnetic field around Io [17] suggested the presence of an electrically conductive subsurface layer, consistent with an internal magma ocean. However, this interpretation has been disfavoured by subsequent reanalysis of the induced magnetic-field data [18], observations of Io's aurora [19] and, most conclusively, by the gravitational signature of Io's tidal deformation measured by the Juno spacecraft [20]. A significant fraction of Io's mantle is therefore partially molten, a state in which the rock comprises two phases: a porous skeleton of solid grains interpenetrated by liquid melt.

In partially molten material (e.g. silicate rock), melt segregates by porous flow, driven by pressure gradients and body forces. This is described by a modified Darcy's law. The long-term, creeping deformation of the residual solid is viscous, including its compaction in response to melt segregation. This is described by a modified Stokes force-balance equation. The coupling of the Darcy and Stokes equations is referred to as poro-viscous compaction theory [6,21]. An associated rheological model supplies viscosities for deviatoric (shear) and isotropic (compaction) viscous deformation. This theory has long been applied to partially molten regions of Earth's mantle [22,23], and also to terrestrial ice [24–26]. Distinct from the terrestrial case, however, the energy that melts Io's interior is that dissipated as heat by tides [4]. Recent work considers the coupled melting, melt segregation and viscous compaction of Io's mantle [27–30], but no work has self-consistently coupled tidal deformation and heat generation with melting [31].

Friction associated with Io's repeated tidal distortion releases heat as Jupiter's gravity field periodically deforms the body into a triaxial figure. Tidal heating has classically been modelled by treating Io's mantle with viscoelastic dissipation theory [32], which partially stems back to the classic work of Love [33]. A key prediction of such modelling is that tidal heat input is spatially variable, with different heat distributions possible depending on internal structure [34]. Melting must also therefore be spatially variable. Melt lubricates grain boundaries, lowering the shear viscosity of the mantle [35]. This means that regions of high melt fraction have lower viscosity and are more susceptible to tidal heating [36]. There is thus an inherent coupling between melt and tidal heat generation. Furthermore, tidally induced deformation of Io's mantle drives melt segregation through (de)compaction. This segregation alters Io's tidal response and drives heating through Darcy flow and viscous compaction. Ref. [37] models the latter process, but treats Io's mantle as a single-phase (solid) material. Hence, [37]'s approach cannot self-consistently take into account melt segregation. A better approach to closing (and understanding) Io's heat budget, is therefore to combine poro-viscous and viscoelastic theories.

The first poro-viscoelastic model of tidal deformation was published in [38] to quantify heating in the porous core of Saturn's icy moon, Enceladus. That work reduced the problem to a kinematic one, whereby the two-phase core was forced by imposed displacements at its surface. Later, [39] improved upon this by imposing appropriate boundary conditions, forcing the core with the tidal potential, and coupling fluid displacements to the gravity field. Most recently, [40] provided a more comprehensive derivation of poro-viscoelastic gravitational dynamics, including detailed consideration of the problem in several limiting cases, noting inconsistencies in both [38,39], and considering radial porosity variations. There are, however, two main deficiencies in all of these works. Firstly, viscous compaction is neglected, despite the fact that it is relevant at the same time scales as viscous shear. Secondly, rheological properties are assumed to be laterally uniform (also a common assumption in one-phase tidal deformation models). For the reasons outlined above, a theory of Io that can plausibly address the ensemble of observations must include both of these

effects. Toward this end, here we incorporate viscous compaction while leaving laterally varying properties for future work.

We model the tidal deformation of Io by treating its interior as a poro-viscoelastic continuum and solving the deformation equations of a self-gravitating body [32], described by the two-phase theory developed in [39,40]. We extend the theory by (i) modifying the isotropic component of the rheological model to self-consistently account for isotropic viscous deformation and (ii) formulating the constitutive laws in a physically and mathematically consistent manner based on the original work of Love [33]. We treat Io's asthenosphere as a two-phase, Maxwell material with impermeable boundaries above and below, exploring how tidal forcing circulates melt in the asthenosphere and dissipates heat due to solid deformation (deviatoric and isotropic) as well as porous flow. We find that dissipation due to (de)compaction can be at most 1–10% of Io's observed heating rate, but the upper end of this range requires an effective grain size greater than or approximately equal to 10 cm. We also find that dissipation from porous flow can generate substantial heating only for a highly permeable asthenosphere, and this state may be possible if, again, the mantle's effective grain size is greater than or approximately equal to 10 cm.

The manuscript is organized as follows. In §2, we describe the theory of poro-viscoelasticity in a compacting, self-gravitating body and our approach to the problem. The relevant internal structures and material parameters of Io are outlined in §3, and corresponding tidal deformation and heating results are given in §4. We summarize the potential next steps for this work in §5, before concluding in §6.

2. Theory

Here, we recap the theory of two-phase mechanics of a self-gravitating, poro-viscoelastic planetary body. The theory builds on the recent developments by [38–40]; the latter two papers are hereafter referred to as RN22 and K23, respectively. We largely formulate the problem following K23, but base the rheological formalism on the original arguments of Love [33] and incorporate a compaction viscosity [6]. We show that Love's original formulation of the problem provides an intuitive, natural extension to poro-viscoelasticity that avoids a mathematical ambiguity often present in the literature.

In §2a, we present the governing equations of poro-viscoelastic gravitational dynamics, followed by their linearization and Fourier transform in §2b. Calculation of dissipation from shear, compaction and Darcy deformation is described in §2c.

(a) Governing equations

In the following, we denote quantities relevant to individual phases with the subscripts l (liquid) and s (solid). When multiple phases are present within a layer, each individual phase requires its own set of conservation laws. For mass conservation these are

$$\frac{\partial(\phi\rho_l)}{\partial t} + \nabla\cdot(\phi\rho_l\boldsymbol{v}_l) = \Gamma \tag{2.1a}$$

and

$$\frac{\partial((1-\phi)\rho_s)}{\partial t} + \nabla\cdot((1-\phi)\rho_s\boldsymbol{v}_s) = -\Gamma, \tag{2.1b}$$

where ϕ is the melt fraction, the volume fraction of liquid present within the two-phase material and Γ is the melting rate. We assume that the background melting time scale, which is in part controlled by the rate of mantle upwelling/downwelling, is much greater than the time scale of tidal deformation [41], and henceforth take $\Gamma = 0$. For phase $j = \{l, s\}$, $\boldsymbol{v}_j$ is the velocity and ρ_j is the density. Summing the above two equations gives the conservation of mass for the phase aggregate in terms of the phase-averaged density, $\rho = (1-\phi)\rho_s + \phi\rho_l$.

royalsocietypublishing.org/journal/rspa Proc. R. Soc. A 481: 20250607

Neglecting inertial terms, the force balance equations for the solid and liquid phases are [39]

$$\nabla \cdot (\phi \boldsymbol{\sigma}_l) - \phi \rho_l \nabla \Phi - \phi \frac{\eta_l}{k} \boldsymbol{q} + p_l \nabla \phi = 0 \tag{2.2a}$$

and

$$\nabla \cdot ((1-\phi)\boldsymbol{\sigma}_s) - (1-\phi)\rho_s \nabla \Phi + \phi \frac{\eta_l}{k} \boldsymbol{q} - p_l \nabla \phi = 0, \tag{2.2b}$$

where $\boldsymbol{\sigma}_l$ and $\boldsymbol{\sigma}_s$ are the liquid and solid stress tensors, respectively, Φ is the sum of all gravitational potentials, k is the permeability of the solid skeleton, η_l is the dynamic viscosity of the melt and $\boldsymbol{q} \equiv \phi(\boldsymbol{v}_l - \boldsymbol{v}_s)$ is the segregation flux. The second term in each equation represents the forces per unit volume of self- and external-gravitation, and the sum of the last two terms is known as the interphase force, $\boldsymbol{F} \equiv (\phi \eta_l / k)\boldsymbol{q} - p_l \nabla \phi$, the equal-and-opposite force per unit volume imposed by the melt on the solid phase [21]. The first term, the divergence of the solid and liquid stresses, balances the gravitation and interphase forces. Summing equations (2.2*a*) and (2.2*b*) cancels the interphase force and yields the force balance for the bulk mixture,

$$\nabla \cdot \boldsymbol{\sigma} - \rho \nabla \Phi = 0, \tag{2.3}$$

where the total stress is given by the volume-averaged sum of the solid and liquid stress tensors,

$$\boldsymbol{\sigma} = (1-\phi)\boldsymbol{\sigma}_s + \phi \boldsymbol{\sigma}_l. \tag{2.4}$$

For shorthand, we sometimes denote the mean total stress as $\sigma \equiv \mathrm{tr}(\boldsymbol{\sigma})/3 = -p$, where p is the total pressure. The permeable solid skeleton is assumed to be isotropically tortuous such that stresses in the fluid are also isotropic,

$$\boldsymbol{\sigma}_l = -p_l \mathbf{1}, \tag{2.5}$$

where $p_l \equiv -\mathrm{tr}(\boldsymbol{\sigma}_l)/3$ is the pore pressure and $\mathbf{1}$ is the identity matrix. The pore pressure is experienced by both the fluid and the solid grains as they are immersed in melt.

Inserting equation (2.5) into equation (2.2*a*) converts the melt's force balance into a modified form of Darcy's law,

$$\boldsymbol{q} = -M_\phi (\nabla p_l + \rho_l \nabla \Phi), \tag{2.6}$$

where we have introduced the fluid's mobility, the ratio of permeability to liquid viscosity,

$$M_\phi \equiv \frac{k(\phi)}{\eta_l}. \tag{2.7}$$

For a given pressure and gravitational forcing, a higher mobility results in a higher segregation flux. Mobility thus quantifies the liquid viscous resistance to melt circulation. We assume that $\eta_l = 1$ Pa s, giving mobility and permeability a 1:1 correspondence throughout the manuscript. The mobility is a function of porosity due to the inherent dependence of permeability on the pore-fraction of the mantle, which we examine further in §4c.

The strain of the material is defined as

$$\boldsymbol{\epsilon}_j \equiv \frac{1}{2}\left[\nabla \boldsymbol{u}_j + (\nabla \boldsymbol{u}_j)^T\right], \tag{2.8}$$

where $\boldsymbol{u}_j$ is the displacement of the solid ($j = s$) or liquid ($j = l$) relative to the pre-stressed, undeformed state. The deformation (strain) of the material must now be linked to the stress it is subjected to via a constitutive law, which describes the stress response of the two-phase material to viscous and elastic strains.

In the poro-viscous limit, the resistance to viscous (de)compaction is governed by the compaction viscosity, ζ. This viscosity depends on both the melt fraction and shear viscosity of the two-phase aggregate (see §4c). In the poroelastic limit, the resistance to elastic compaction is governed by the compaction modulus, κ_d, which is sometimes known as the drained bulk modulus and also depends on melt fraction. The compaction modulus is distinct from the bulk modulus of the solid grains, κ_s, because a two-phase material with incompressible solid grains can nonetheless compact elastically—by expelling or imbibing melt. The ratio of the compaction and bulk moduli is quantified by Biot's coefficient, α, a constant that describes the compliance of

the solid skeleton relative to the solid grains under isotropic stresses. Biot's coefficient is defined as

$$\alpha \equiv 1 - \frac{\kappa_d}{\kappa_s}, \tag{2.9}$$

which is relevant for only elastic compaction. When $\alpha = 0$, the solid skeleton is as incompressible as the solid grains themselves, meaning that the skeleton is strong and effective at elastically resisting isotropic stresses. If $\alpha = 1$, the solid grains are incompressible and, relative to this, the skeleton is weak against isotropic stresses. As described next, we incorporate both viscous and elastic compaction behaviour in our constitutive law.

Forming a mechanically consistent constitutive law in the context of a two-phase material is less clear than for a single-phase material. It is therefore important to carefully formulate the problem, which we do following the original arguments presented in Chapter VII of [33]. The key argument made by Love [33] is that, upon displacement, a material element carries with it (i.e. advects) its initial hydrostatic stress. This motivates defining a constitutive law using material derivatives of the stress. For a two-phase material, extra caution is required; the solid and liquid phases that occupy a volume element in the deformed state may originate from different positions, thus carrying with them different hydrostatic pressures (even if the liquid and solid densities are equal). In electronic supplementary material, S1, we apply Love's argument to both poro-viscous and poroelastic rheological laws to derive an appropriate poro-viscoelastic constitutive law that captures advection of both the solid and liquid hydrostatic pressure fields. Our constitutive law for a compacting poro-viscoelastic Maxwell material is [37,39,40,42]

$$\begin{aligned}(1-\phi)\left[\frac{\mathrm{D}_s\boldsymbol{\sigma}_s}{\mathrm{D}t} + \frac{1}{3}\frac{\kappa_d}{\zeta}\int_t \frac{\mathrm{D}_s \mathrm{tr}(\boldsymbol{\sigma}_s)}{\mathrm{D}t}\,\mathrm{d}t\mathbf{1}\right] + \left[(\alpha-\phi)\frac{\mathrm{D}_l p_l}{\mathrm{D}t} + (1-\phi)\frac{\kappa_d}{\zeta}\int_t \frac{\mathrm{D}_l p_l}{\mathrm{D}t}\,\mathrm{d}t\right]\mathbf{1} \\ + (1-\phi)\frac{\mu}{\eta}\left[\boldsymbol{\sigma}_s - \frac{1}{3}\mathrm{tr}(\boldsymbol{\sigma}_s)\mathbf{1}\right] = \lambda_d \mathrm{tr}(\dot{\boldsymbol{\epsilon}}_s)\mathbf{1} + 2\mu\dot{\boldsymbol{\epsilon}}_s,\end{aligned} \tag{2.10}$$

where t is time, μ is the elastic shear modulus, $\lambda_d = \kappa_d - 2\mu/3$ and η, ζ are the shear and compaction viscosities, respectively, which control the anelastic delay in the response of the two-phase material to shear and isotropic stresses. The Lagrangian derivatives for material phase $j = \{s, l\}$ are defined as

$$\frac{D_j}{Dt} \equiv \frac{\partial}{\partial t} + \boldsymbol{v}_j \cdot \boldsymbol{\nabla}, \tag{2.11}$$

and their appearance in equation (2.10) is a result of applying Love's argument. Equation (2.10) reduces to the constitutive law used in RN22 and K23 when $\zeta \to \infty$ (no viscous compaction) and when advective terms in the Lagrangian derivatives are neglected. The constitutive law in eqn. (6) of [37] is recovered when there is no melt ($\alpha = \phi = 0$) and advective terms are neglected. The benefit and mathematical consistency of formulating the constitutive law with Lagrangian derivatives will become clear in the next section when the equations are linearized.

The law relating the strain of the fluid to the liquid stress tensor can be derived using the following equations of state [43,44]:

$$\frac{\mathrm{d}\rho_l}{\rho_l} = \frac{\mathrm{d}p_l}{\kappa_l} \tag{2.12a}$$

and

$$\frac{\mathrm{d}\rho_s}{\rho_s} = \frac{1}{\kappa_s}\left[\frac{1}{1-\phi}\,\mathrm{d}p^d + \mathrm{d}p_l\right], \tag{2.12b}$$

where $p^d \equiv -\sigma - p_l$ is the differential between the total pressure and the pore pressure, and κ_l is the bulk modulus of the liquid. Summing the liquid and solid continuity equations (2.1) and using the above equations of state equations (2.12) yields the storage equation,

$$\phi\left[\frac{1}{\kappa_l} - \frac{1}{\kappa_s}\right]\frac{\mathrm{D}_l p_l}{\mathrm{D}t} + \frac{1}{\kappa_l}\boldsymbol{q}\cdot\boldsymbol{\nabla}p_l - \frac{1}{\kappa_s}\frac{\mathrm{D}_s\sigma}{\mathrm{D}t} + \boldsymbol{\nabla}\cdot\boldsymbol{q} + \boldsymbol{\nabla}\cdot\boldsymbol{v}_s = 0, \tag{2.13}$$

which we give in terms of the mean total stress σ. If we neglect all advective terms and assume that the two-phase material behaves elastically under isotropic stresses ($\zeta \to \infty$), then taking the

trace of equation (2.10) gives $\dot{\sigma} = \kappa_d \mathrm{tr}(\dot{\boldsymbol{\epsilon}}_s) + \alpha \dot{p}_l$, and $\boldsymbol{\nabla} \cdot \boldsymbol{v}_s = \mathrm{tr}(\dot{\boldsymbol{\epsilon}}_s)$, so equation (2.13) reduces to

$$S \frac{\partial p_l}{\partial t} + \alpha \mathrm{tr}(\dot{\boldsymbol{\epsilon}}_s) = -\boldsymbol{\nabla} \cdot \boldsymbol{q} \quad \text{(elastic isotropic deformation, } \zeta \to \infty\text{)}, \tag{2.14}$$

where S is the storativity,

$$S \equiv \frac{\phi}{\kappa_l} + (\alpha - \phi)\frac{1}{\kappa_s}, \tag{2.15}$$

the inverse of which is referred to as Biot's modulus [40,45]. Equation (2.14) states that the compression of the liquid and solid on the left-hand side is balanced by changes in the relative volume flux of liquid entering or leaving the reference volume. We can see that if the melt becomes increasingly immobile, $\boldsymbol{q} \to \boldsymbol{0}$, then the right-hand side goes to zero and the pore pressure is dependent only on compaction of the solid skeleton. Integrating this expression with respect to time, assuming porosity is constant, and rearranging yields eqn. (3) in K23 and eqn. (17) in RN22 when written in terms of the variation of fluid content, $\phi \boldsymbol{\nabla} \cdot (\boldsymbol{u}_l - \boldsymbol{u}_s)$. We note that while K23 does consider radial porosity variation throughout their manuscript, these variations are neglected in their storage equation. Following traditional poroelasticity, both RN22 and K23 do not include advective terms in their storage equations. However, we proceed without neglecting the advective terms in equation (2.13); they originate from the material derivatives within the continuity equations, and therefore are essential in accounting for self-gravity and advection of hydrostatic stresses [33].

As we are interested in the more general storage equation that includes viscous compaction (finite ζ) and advection of hydrostatic stress, we cannot easily time-integrate equation (2.13) because of the integral terms present in equation (2.10). We can only further simplify the storage equation in the Fourier domain (§2b).

Finally, Poisson's equation for the gravitational potential Φ depends on the density of the mixture,

$$\nabla^2 \Phi = 4\pi G \rho, \tag{2.16}$$

where G is the universal gravitational constant. This equation must be solved everywhere.

The equations presented here all reduce to the standard solid-body deformation equations when $\phi = 0$ and $\alpha = 0$ [32,46]. Moderate simplification of the problem can be made by assuming incompressibility. If the solid is incompressible ($\kappa_s \to \infty$), then $\alpha \to 1$ and $S \to \phi/\kappa_l$. If only the liquid is incompressible ($\kappa_l \to \infty$), then $S \to (\alpha - \phi)/\kappa_s$. Assuming both phases are incompressible, the storage equation (2.13) expresses mass conservation due to only segregation, $\boldsymbol{\nabla} \cdot (\phi \boldsymbol{v}_l) = -\boldsymbol{\nabla} \cdot (1 - \phi)\boldsymbol{v}_s$. Even if both phases are incompressible, the compaction modulus of the two-phase aggregate can remain finite, meaning that the skeleton can still undergo volume changes due to expulsion/imbibition of melt.

(b) Linearization and fourier transform

In this section we linearize the dynamics that govern equations (2.1*a*), (2.1*b*), (2.3), (2.6), (2.10), (2.13) and (2.16). We denote the base state with subscript 0 and the perturbed (deformed) state with subscript 1. The base state is assumed to be at rest, in hydrostatic equilibrium, and spherically symmetric such that it is only dependent on the radial coordinate $r = |\boldsymbol{r}|$. As the base state has $\boldsymbol{v}_0 = \boldsymbol{0}$, we omit the 1 subscript for $\boldsymbol{v}_j$ and $\boldsymbol{u}_j$, though they remain first-order quantities. The perturbed quantities can vary in three-dimensional space and so are functions of the position vector. That is, for any unknown f_j of material phase $j = \{s, l\}$,

$$f_j(\boldsymbol{r}, t) = f_{j,0}(r) + f_{j,1}(\boldsymbol{r}, t). \tag{2.17}$$

The initial position of the material within the volume element at position $\boldsymbol{r}$ is less clear in the multi-phase problem than in the single-phase one. The subtlety to recognize is that the initial

position of the material within that element can only be recovered through the displacement of the *corresponding material phase j*. The phase-dependent initial position $\boldsymbol{r}_{j,0}$ is thus recovered through

$$\boldsymbol{r} = \boldsymbol{r}_{j,0} + \boldsymbol{u}_j. \tag{2.18}$$

This approach is a natural extension of the argument made by Love [33] to the two-phase problem, and is crucial in ensuring mechanical consistency in the problem.

In the following, we take particular care in linearizing the constitutive laws (equations (2.10) and (2.13)) as we form these in a different manner to previous works. When needed, the linearized equations are converted into the Fourier domain by assuming time-periodic solutions of the form

$$f_{j,1} = \tilde{f}_{j,1}\, \mathrm{e}^{\mathrm{i}\omega t}, \tag{2.19}$$

where $\tilde{f}_j$ is the complex Fourier-transformed variable of material phase j, the forcing frequency is ω, and i is the imaginary number.

Expanding the density field in the form of equation (2.17) gives

$$\rho_j(\boldsymbol{r}, t) = \rho_{j,0}(r) + \rho_{j,1}(\boldsymbol{r}, t). \tag{2.20}$$

Inserting this into the conservation of mass equations (2.1), neglecting second-order terms in perturbed quantities, and integrating with respect to time gives the density perturbations,

$$\phi\rho_{l,1} = -\boldsymbol{u}_l \cdot \boldsymbol{\nabla}(\phi\rho_{l,0}) - \phi\rho_{l,0}\boldsymbol{\nabla} \cdot \boldsymbol{u}_l \tag{2.21a}$$

and

$$(1-\phi)\rho_{s,1} = -\boldsymbol{u}_s \cdot \boldsymbol{\nabla}[(1-\phi)\rho_{s,0}] - (1-\phi)\rho_{s,0}\boldsymbol{\nabla} \cdot \boldsymbol{u}_s, \tag{2.21b}$$

where we have assumed that porosity is constant (discussed in electronic supplementary material, S2). The density perturbations thus consist of two parts: a perturbation due to advection of the base state, and a perturbation due to compression or expansion of the solid or liquid. The advection term is critical to account for alteration of the gravitational potential due to mass redistribution.

Expanding the gravitational potential in the form of equation (2.17) gives

$$\Phi(\boldsymbol{r}, t) = \Phi_0(r) + \Phi_1(\boldsymbol{r}, t), \tag{2.22}$$

where Φ_0 is the pre-stressed gravitational potential of the body. At rest and in the absence of tidal forcing, Poisson's equation (2.16) for the base state gravitational potential integrates to

$$\nabla\Phi_0(r) = g(r)\boldsymbol{e}_r, \tag{2.23}$$

where $\boldsymbol{e}_r$ is the radial basis vector and $g(r) = G\int_V \rho\, \mathrm{d}V/r^2$, where V is the spherical volume of radius r. Poisson's equation for the gravitational perturbation is found by inserting equations (2.22) and (2.21) into equation (2.16):

$$\nabla^2\Phi_1 = -4\pi G[u_s^r \partial_r\rho_0 + \rho_0\boldsymbol{\nabla} \cdot \boldsymbol{u}_s + u_{\mathrm{rel}}^r \partial_r(\phi\rho_{l,0}) + \phi\rho_{l,0}\boldsymbol{\nabla} \cdot \boldsymbol{u}_{rel}], \tag{2.24}$$

where $\boldsymbol{u}_{rel} \equiv \boldsymbol{u}_l - \boldsymbol{u}_s$ is the relative/segregation displacement, superscript r indicates a radial vector component and ∂_r is the partial derivative with respect to radius. This expression is equivalent to eqn. (21) in K23, and eqn. (33) in RN22 under the assumption of uniform layer density and melt fraction.

The solid Cauchy stress tensor and pore pressure are decomposed identically to equation (2.17):

$$\boldsymbol{\sigma}_s(\boldsymbol{r}, t) = \boldsymbol{\sigma}_{s,0}(r) + \boldsymbol{\sigma}_{s,1}(\boldsymbol{r}, t) \tag{2.25a}$$

and

$$p_l(\boldsymbol{r}, t) = p_{l,0}(r) + p_{l,1}(\boldsymbol{r}, t), \tag{2.25b}$$

which consists of only the hydrostatic base state and a perturbation due to deformation. The decomposition in equation (2.25) is identical to the decomposition of Φ and ρ_j, which we emphasize is a different approach to most tidal deformation texts where an advective term is

forced into the decomposition [46]. Below, we show that the approach used here reproduces the classic tidal deformation equations because material advection is naturally accounted for in our constitutive laws (equations (2.10) and (2.13)).

At rest ($p_l = p_{l,0}$, $\boldsymbol{\sigma}_s = \boldsymbol{\sigma}_{s,0}$, $\boldsymbol{\sigma} = \boldsymbol{\sigma}_0$) and using equations (2.5) and (2.23), the liquid, solid and bulk momentum equations (2.2) and (2.3) reduce to hydrostatic balance,

$$-\nabla p_{l,0} = \rho_{l,0} g \boldsymbol{e}_r, \tag{2.26a}$$

$$-\nabla p_{s,0} = \rho_{s,0} g \boldsymbol{e}_r \tag{2.26b}$$

and

$$\nabla \cdot \boldsymbol{\sigma}_0 = -\nabla p_0 = \rho_0 g \boldsymbol{e}_r, \tag{2.26c}$$

where in equation (2.26*b*) we have assumed that porosity is a constant.

Inserting equation (2.25) into the solid constitutive law (equation (2.10)), neglecting second-order terms in perturbed quantities, and assuming hydrostatic balance in the base state by inserting equation (2.26) gives

$$\dot{\boldsymbol{\sigma}}_1 + \alpha \dot{p}_{l,1}\mathbf{1} + [(\rho_0 - \alpha\rho_{l,0})v_s^r - (\alpha - \phi)v_{rel}^r \rho_{l,0}]g\mathbf{1} + \frac{\mu}{\eta}\left[\boldsymbol{\sigma}_1 - \frac{1}{3}\mathrm{tr}(\boldsymbol{\sigma}_1)\mathbf{1}\right] + \frac{\kappa_d}{\zeta}\left[\frac{1}{3}\mathrm{tr}(\boldsymbol{\sigma}_1) + p_{l,1} + (\rho_0 - \phi\rho_{l,0})u_s^r g - (1-\phi)u_{rel}^r \rho_{l,0} g\right]\mathbf{1} = \lambda_d \mathrm{tr}(\dot{\boldsymbol{\epsilon}}_s)\mathbf{1} + 2\mu\dot{\boldsymbol{\epsilon}}_s, \tag{2.27}$$

which is written in terms of the total stress perturbation and solid and relative velocities and displacements. Here, overdots represent partial time derivatives, $\partial/\partial t$. This equation is more compact in the frequency domain; taking the Fourier transform of equation (2.27) and rearranging gives

$$\tilde{\boldsymbol{\sigma}}_1 = \left[\tilde{\kappa}_d - \frac{2}{3}\tilde{\mu}\right]\mathrm{tr}(\tilde{\boldsymbol{\epsilon}}_s)\mathbf{1} + 2\tilde{\mu}\tilde{\boldsymbol{\epsilon}}_s - \tilde{\alpha}\tilde{p}_{l,1}\mathbf{1} - [(\rho_0 - \tilde{\alpha}\rho_{l,0})\tilde{u}_s^r - (\tilde{\alpha} - \phi)\tilde{u}_{rel}^r \rho_{l,0}]g\mathbf{1}, \tag{2.28}$$

where the complex shear modulus, drained compaction modulus and Biot's coefficient are

$$\tilde{\mu} \equiv \frac{i\omega\mu}{i\omega + \mu/\eta}, \tag{2.29a}$$

$$\tilde{\kappa}_d \equiv \frac{i\omega\kappa_d}{i\omega + \kappa_d/\zeta} \tag{2.29b}$$

and

$$\tilde{\alpha} \equiv 1 - \frac{\tilde{\kappa}_d}{\kappa_s}, \tag{2.29c}$$

respectively. The mean total stress perturbation is given by the trace of equation (2.28),

$$\mathrm{tr}(\tilde{\boldsymbol{\sigma}}_1)/3 = \tilde{\sigma}_1 = \tilde{\kappa}_d \mathrm{tr}(\tilde{\boldsymbol{\epsilon}}_s) - \tilde{\alpha}\tilde{p}_{l,1} - [(\rho_0 - \tilde{\alpha}\rho_{l,0})\tilde{u}_s^r - (\tilde{\alpha} - \phi)\tilde{u}_{rel}^r \rho_{l,0}]g. \tag{2.30a}$$

Next, we linearize the storage equation in equation (2.13) and insert equations (2.26*a*) and (2.26*c*):

$$\left[\frac{\phi}{\kappa_l} - \frac{\phi}{\kappa_s}\right][\dot{p}_{l,1} - v_l^r \rho_{l,0} g] = \frac{\phi}{\kappa_s} v_{rel}^r \rho_{l,0} g + \frac{1}{\kappa_s}[\dot{\sigma}_1 + \rho_0 v_s^r g] - \phi\mathrm{tr}(\dot{\boldsymbol{\epsilon}}_{rel}) - \mathrm{tr}(\dot{\boldsymbol{\epsilon}}_s), \tag{2.31}$$

where $\dot{\sigma}_1$ is obtained by taking one third the trace of equation (2.27) (see electronic supplementary material, S3). Assuming Fourier solutions of the form in equation (2.19) for equation (2.31), inserting equation (2.30*a*) and rearranging gives

$$\tilde{p}_{l,1} = \tilde{u}_l^r \rho_{l,0} g - \tilde{S}^{-1}[\tilde{\alpha}\mathrm{tr}(\tilde{\boldsymbol{\epsilon}}_s) + \phi\mathrm{tr}(\tilde{\boldsymbol{\epsilon}}_{rel})], \tag{2.32}$$

where the complex storativity is

$$\tilde{S} \equiv \frac{\phi}{\kappa_l} + (\tilde{\alpha} - \phi)\frac{1}{\kappa_s}. \tag{2.33}$$

For later convenience and easier comparison to existing work, we write the pore pressure perturbation as

$$\tilde{p}_{l,1} = \tilde{u}_l^r \rho_{l,0} g + \tilde{p}_{l,1}^{\delta}, \tag{2.34a}$$

where the non-advective portion of the liquid stress is defined as

$$\tilde{p}^{\delta}_{l,1} \equiv -\tilde{S}^{-1}[\tilde{\alpha}\,\mathrm{tr}(\tilde{\boldsymbol{\epsilon}}_s) + \phi\,\mathrm{tr}(\tilde{\boldsymbol{\epsilon}}_{rel})]. \tag{2.34b}$$

Equation (2.34*b*) is equivalent to eqn. (6) in K23 if compaction is ignored ($\zeta \to \infty$). We can then insert equation (2.34*a*) into the linearized frequency-domain solid constitutive law, equation (2.28), which simplifies to

$$\tilde{\boldsymbol{\sigma}}_1 = -[\rho_0 \tilde{u}^r_s + \phi \tilde{u}^r_{rel}\rho_{l,0}]g\mathbf{1} + \tilde{\boldsymbol{\sigma}}^{\delta}_1, \tag{2.35a}$$

where we have defined the non-advective stress perturbation,

$$\tilde{\boldsymbol{\sigma}}^{\delta}_1 \equiv \left[\tilde{\kappa}_d - \frac{2}{3}\tilde{\mu}\right]\mathrm{tr}(\tilde{\boldsymbol{\epsilon}}_s)\mathbf{1} + 2\tilde{\mu}\tilde{\boldsymbol{\epsilon}}_s - \tilde{\alpha}\tilde{p}^{\delta}_{l,1}\mathbf{1}. \tag{2.35b}$$

Equation (2.35*a*) is the frequency-domain poro-viscoelastic constitutive law that includes advection of the hydrostatic base state pressure field, and is equivalent to eqn. (41) in K23. As expected from the correspondence principle, equations (2.35*a*) and (2.35*b*) are analogous to the poroelastic problem in the time domain. If there is no melt, $\phi = 0$, $\kappa_d = \kappa_s$, and therefore $\alpha = 0$, equation (2.35) reduces to the elastic constitutive law in eqn. (6), Chapter VII of [33].

Now that we have a frequency-domain constitutive law for the liquid and solid (equations (2.34*a*), (2.34), (2.35)), we can proceed to linearize and Fourier transform the momentum equations.

The linearized frequency-domain liquid momentum equation is obtained by substituting equations (2.5), (2.20), (2.21), (2.22), (2.24), (2.25), (2.26*a*) and (2.34*a*) into the Fourier transform of Darcy's law in equation (2.6). Neglecting second-order terms in perturbed quantities, this gives

$$i\omega\phi\tilde{\boldsymbol{u}}_{rel} = -M_\phi[\rho_{l,0}\partial_r(g\tilde{u}^r_l)\boldsymbol{e}_r + \nabla\tilde{p}^{\delta}_{l,1} + \rho_{l,0}\nabla\tilde{\Phi}_1 - \rho_{l,0}g(\nabla\cdot\tilde{\boldsymbol{u}}_l)\boldsymbol{e}_r], \tag{2.36}$$

which is a form of Darcy's law that accounts for compression and self-gravity of the circulating melt. Equation (2.36) is identical to eqn. (49) in K23 when ignoring inertial terms, radial variations in porosity, and setting $u^r_l = u^r_{rel} + u^r_s$ and $\nabla\cdot\tilde{\boldsymbol{u}}_l = \mathrm{tr}(\tilde{\boldsymbol{\epsilon}}_s + \tilde{\boldsymbol{\epsilon}}_{rel})$. As noted in K23, this differs from the Fourier transform of eqn. (29b) in RN22 because advection of the base state pressure and density fields was neglected. We show in electronic supplementary material S7 that this leads to slightly incorrect energy dissipation rates.

Following the same procedure for the Fourier transform of the momentum equation of the bulk mixture (equation 2.3) gives

$$\nabla\cdot\tilde{\boldsymbol{\sigma}}^{\delta}_1 = \rho_0\partial_r(g\tilde{u}^r_s)\boldsymbol{e}_r + \phi\rho_{l,0}\partial_r(g\tilde{u}^r_{rel})\boldsymbol{e}_r + \rho_0\nabla\tilde{\Phi}_1 - [\rho_0\nabla\cdot\tilde{\boldsymbol{u}}_s + \phi\rho_{l,0}\nabla\cdot\tilde{\boldsymbol{u}}_{rel}]g\boldsymbol{e}_r. \tag{2.37}$$

This equation is identical to eqn. (48) in K23 if inertial terms are neglected. Moreover, our equation (2.37) differs from the Fourier transform of RN22 eqn. (29a) because advection of the base state pressure and density fields was neglected. In their case, eqn. (29a) in RN22 does not reduce to the classic, solid-body, linearized momentum equation if $\phi = \rho_l = 0$ (eqn. 1.58 in [46]). This is because of the assumption of uniform layer density in RN22.

Despite having formulated the solid and liquid constitutive laws to explicitly include material advection—a different approach to most tidal deformation studies—we have arrived at the same set of linearized momentum equations. We argue that this approach, which is simply an extension of the classic elastic approach by Love [33] to the viscoelastic and poro-viscoelastic problems, is more physically intuitive and mathematically consistent than that outlined in, for example, [46]. This consistency is the inclusion of material advection in our constitutive laws, which avoids the need to make an ad hoc assumption about why stresses should be linearized differently to other problem variables, as is commonly done.

The governing equations have now been linearized and converted to the frequency domain (equation (2.24), (2.34), (2.35), (2.36) and (2.37)). To solve these coupled equations, the unknown quantities are expanded in spherical harmonics, converted to a set of ordinary differential equations in radius and then numerically integrated. Details regarding this are well documented

in the literature; we provide further information in the electronic supplementary material, S4 and S5.

(c) Dissipation

After the tidal response of Io is computed, we determine the tidal dissipation rate throughout the body. The dissipation rate is inherently related to the time delay in the response of the body to the forcing potential, and is thus dependent on the imaginary parts of the complex rheological parameters, $\tilde{\mu}$, $\tilde{\kappa}_d$, $\tilde{S}$, as well as M_ϕ.

The forcing period-averaged dissipation rate per unit volume is [38]

$$\dot{E}^v = \frac{1}{P}\int_P \underbrace{\boldsymbol{\sigma}_1 : \dot{\boldsymbol{\epsilon}}_s - \phi p_l \mathrm{tr}(\dot{\boldsymbol{\epsilon}}_{rel})}_{\text{solid}} + \underbrace{\frac{\boldsymbol{q}\cdot\boldsymbol{q}}{M_\phi}}_{\text{liquid}} \,\mathrm{d}t, \tag{2.38}$$

where Io's 42 hr forcing period is $P = 2\pi/\omega$. The first two terms on the right-hand represent dissipation due to shear and compaction of the solid skeleton itself. The last term accounts for viscous heating in the melt, otherwise known as Darcy dissipation. We refer to heating from isotropic deformation as *compaction* dissipation, rather than the commonly used bulk dissipation [37]. This choice avoids the notion that heating from isotropic deformation is a phase- or spatially averaged quantity, such as the bulk density. Similar to K23, we can split this dissipation rate into contributions from shearing $\dot{E}^v_S$, compaction $\dot{E}^v_C$, and (viscous) Darcy flow due to fluid–solid segregation $\dot{E}^v_D$:

$$\dot{E}^v_S = -\Omega \mathrm{Im}(\tilde{\mu})\left[|\tilde{\epsilon}_{rr}|^2 + |\tilde{\epsilon}_{\theta\theta}|^2 + |\tilde{\epsilon}_{\varphi\varphi}|^2 + 2|\tilde{\epsilon}_{r\theta}|^2 + 2|\tilde{\epsilon}_{r\varphi}|^2 + 2|\tilde{\epsilon}_{\theta\varphi}|^2 - \frac{1}{3}|\mathrm{tr}(\boldsymbol{\epsilon}_s)|^2\right], \tag{2.39a}$$

$$\dot{E}^v_C = -\frac{\Omega}{2}\mathrm{Im}(\tilde{\kappa}_d)\left[|\mathrm{tr}(\tilde{\boldsymbol{\epsilon}}_s)|^2 + \left|\frac{\tilde{p}_l}{\kappa_s}\right|^2\right] \tag{2.39b}$$

and

$$\dot{E}^v_D = \frac{\phi^2\Omega^2}{2}\frac{1}{M_\phi}|\tilde{\boldsymbol{u}}_{rel}|^2, \tag{2.39c}$$

where $\Omega = |\omega|$ is Io's rotation frequency. In contrast to K23, we have combined fluid and solid effects in our expression for compaction dissipation (equation (2.39*a*)). While equation (2.39*b*) contains contributions from both solid deformation and melt, the resulting dissipation only occurs in the solid. Compaction dissipation therefore represents the heating associated with solid-grain rearrangement as pore space is opened/closed. The total time-averaged dissipation rate is the sum of equations (2.39) over the total volume of the body:

$$\dot{E} = \int_V (\dot{E}^v_S + \dot{E}^v_C + \dot{E}^v_D)\,\mathrm{d}V. \tag{2.40}$$

The strain, displacement and pressure magnitudes in equation (2.39) depend on the type, frequency and magnitude of the tidal forcing. We force Io with the time-varying gravitational potential arising from small orbital eccentricity, e, limited to the diurnal (orbital) frequency [47]. We neglect the much smaller forcing due to obliquity and adjacent moons [48,49]. Specific details are given in electronic supplementary material, S6.

The total dissipation rate can also be determined using the phase delay of the gravitational response of the body, given by the imaginary component of the tidal Love number k_2. This can be recovered with the response gravitational potential computed at the surface (see electronic supplementary material, eqn. (S6.2)). For a synchronously rotating body in an eccentric orbit with eccentricity $e \ll 1$, the total dissipation rate is [32]

$$\dot{E} = -\frac{21}{2}\mathrm{Im}(k_2)\frac{\Omega^5 R^5}{G}e^2. \tag{2.41}$$

Table 1. Parameters describing Io's internal structure and corresponding material properties. The compaction modulus κ_d is controlled by α through equations (2.9) or (4.8).

quantity	symbol	units	crust	asthenosphere	lower mantle	core
layer thickness	Δr	km	20	50–400	700–1050	700
solid density	ρ_s	kg m^{-3}	3000	3300	3300	—
liquid density	ρ_l	kg m^{-3}	—	3300	—	7640
shear modulus	μ	GPa	60	60*	60	0
solid bulk modulus	κ_s	GPa	200	200	200	—
liquid bulk modulus	κ_l	GPa	—	1–200	—	200
shear viscosity	η	Pa s	10^{25}	10^{12}–10^{21} *	10^{21}	—
liquid viscosity	η_l	Pa s	—	1	—	0
Biot's coefficient	α	—	—	0.01–1*	—	—
compaction modulus	κ_d	GPa	—	2–200*	—	—
permeability	k	m^2	—	10^{-10}–10^{-3} *	—	—

*Asterisks indicate parameters that can vary with melt fraction.

A crucial check to the numerical solution of the tidal deformation problem is that equations (2.40) and (2.41) give identical results.

Now that the mathematical problem has been posed, we must next define the internal and rheological structure of Io.

3. Internal structure and boundary conditions

Io's internal structure has been constrained through determination of its gravity field, moment of inertia, topography and tidal deformation by the Galileo and Juno spacecraft [20,50,51]. Its inferred moment of inertia is consistent with a differentiated body with metallic iron core [51]. The tidal perturbation of its gravity field is consistent with an interior where the melt fraction is below the disaggregation limit (i.e. $\phi < 0.3$), meaning no shallow magma ocean is present [20,52]. Mountains with relief of 20 km indicate that the lithosphere is strong, despite Io's abundant surface volcanism [53,54]. To respect these constraints while retaining simplicity, we adopt a four-layer internal structure. This structure, listed in table 1, comprises a molten core, solid lower mantle, partially molten asthenosphere and a solid, stiff lithosphere. We assume that the origin of the asthenosphere's melt is localized tidal heating, thus we consider only a 'shallow' mantle model of dissipation, neglecting contributions from the deep mantle [32]. We vary the thickness H and melt fraction ϕ of the asthenosphere, as well as the mobility of the melt–solid aggregate (equation (2.7)) and compressibility of the melt. The solid and melt densities are taken to be equal ($\rho_s = \rho_l$), ensuring that the base state of the asthenosphere is at rest, simplifying our analysis.

We know from observation and modelling that melt must pass from asthenosphere into the lithosphere where it is erupted onto the surface [5,55]. However, over the time scale of diurnal tides, flow in or out of the asthenosphere is probably small. We therefore take the top and bottom boundaries of the asthenosphere to be impenetrable such that $\boldsymbol{q} \cdot \boldsymbol{e}_r = 0$. Melt is thus confined to the asthenosphere in our model. For other possible boundary conditions, see RN22 and K23.

4. Results

In §2, we presented the two-phase theory of gravito-poroviscoelastic dynamics. In this section, we apply the theory to Io, assuming an internal structure as given in §3. To begin, in §4a we gain intuition for the primary controls and broad patterns of Io's two-phase tidal response. For this,

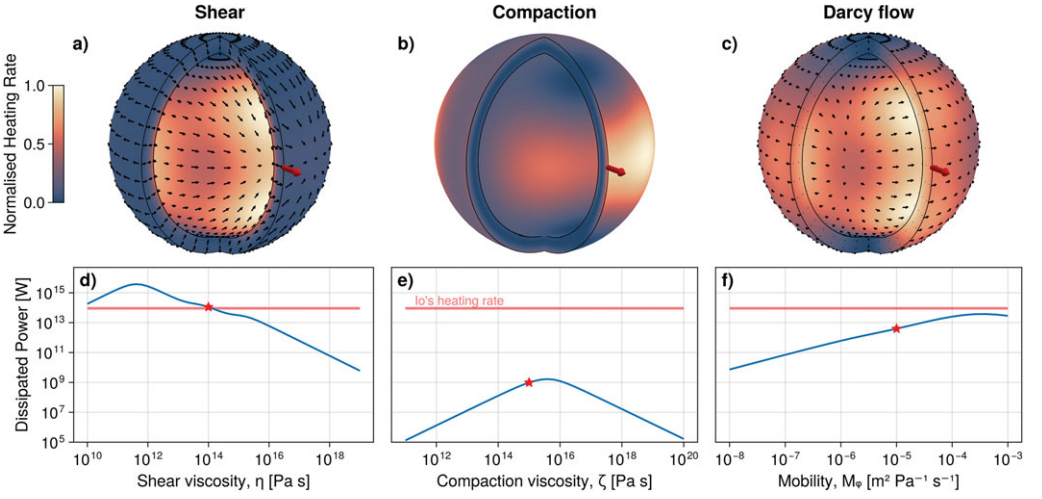

Figure 1. Qualitative tidal deformation solutions of a 300 km thick asthenosphere at perijove ($t = 0$) for deformation due to (a) shear, (b) compaction and (c) melt segregation. The arrows in (a) and (c) indicate the solid and segregation displacements, respectively ($\boldsymbol{u}_s$ and $\boldsymbol{u}_{rel}$), tangent to the surface in which they are plotted. The tidal axis (red arrow) points towards Jupiter. The inner and outer sphere are the base and surface of the asthenosphere, respectively, and the colours represent the period-averaged volumetric heating rate within each surface plotted. Panels (d), (e) and (f) show the total heating rate for shear, compaction, and Darcy flow, respectively, as a function of each mechanism's primary control parameter. Red stars correspond to the solution shown in the top row. Io's observed heating rate (red line) is from [2].

we use a simplified reference case with incompressible solid and liquid phases. In §4b, we relax the incompressibility assumption and determine the sensitivity of the tidal heating solutions to other two-phase control parameters. We then allow the poro-viscoelastic parameters to co-vary as functions of ϕ in §4c. We treat the melt fraction as an input parameter, and assume that it is constant and uniform. Calculations with different values of ϕ enable a more realistic insight into how Io's heat generation might be influenced by its melt fraction. In §4d, we present the spatial patterns of heating associated with each heating mechanism, and how these compare to the distribution of Io's volcanoes. The code to reproduce all figures is available at [56].

(a) Primary controls on tidal deformation and heating

A set of reference, two-phase tidal deformation solutions within an $H = 300\,\text{km}$ thick asthenosphere are shown in figure 1. Here, we assume that each phase is incompressible, $\kappa_l \to \infty$, $\kappa_s \to \infty$, while the two-phase aggregate remains compactible, $\kappa_d = 200\,\text{GPa}$, so that $\alpha \to 1$.

In figure 1a, we see the tidal deformation solutions associated with shear, which is the largest part of Io's tidal deformation. The total heating rate varies with shear viscosity (bottom panel), with a peak close to where the shear Maxwell time $\tau_S = \eta/\mu$ of the asthenosphere approaches the forcing period, typical of many tidal heating studies [32]. The top panel shows the asthenosphere's displacement field with a shear viscosity of $\eta = 10^{14}\,\text{Pa s}$, which reproduces Io's total heating rate (star, bottom panel). This shear viscosity is much lower than that of Earth's mantle, which we discuss further in §5. We see a clear angular separation between the tidal axis (red arrow), and the region of highest tide (area of convergence at the surface). The volumetric tidal heating rate peaks at the base of the asthenosphere, and has a dissipation pattern with maxima at mid-latitudes and zero at the poles, consistent with the 'shallow mantle' model of [32].

Heating due to compaction is shown in figure 1b. Like shear deformation, the total compaction-heating rate peaks at a specific value of ζ. This peak occurs when the *compaction* Maxwell time $\tau_C = \zeta/\kappa_d$ approaches the forcing period. When ζ is high, compaction is dominantly

elastic, and when ζ is low, compaction is viscous. The peak heating rate occurs between these two limits. However, for any ζ, heating from compaction is substantially below Io's observed heating rate. This is a consequence of assuming a fairly incompactible asthenosphere ($\kappa_d = 200\,\text{GPa}$) and incompressible solid and liquid phases, as will be shown in §4b(ii). The time-averaged heating pattern, consistent with [37], is focused towards the equator, peaks either side of the tidal axis and is non-zero at the poles. For this reference case, heating is focused in the shallow asthenosphere, unlike the distribution of shear heating.

Finally, in figure 1c, we see the liquid displacement and heating rates due to Darcy flow (solid–melt segregation). The Darcy displacement at $t = 0$ for $M_\phi = 10^{-5}\,\text{m}^2\,\text{Pa}^{-1}\,\text{s}^{-1}$ is shown in the top row. We see that the melt primarily segregates laterally, flowing (relative to the solid) from one side of the tidal axis to the other. In this reference model, the lateral volumetric heating pattern is similar to that from shear deformation, but is much more uniform over the depth of the asthenosphere. The total Darcy heating rate, shown in the bottom panel, is controlled by the mobility of the melt, M_ϕ. Similarly to shear and compaction, there is a critical mobility at which the Darcy heating rate peaks, with decreasing dissipation to either side of this value. The critical mobility results from a competition between the forces that oppose elastic compaction: viscous stresses in the melt, and elastic resistance of the solid skeleton. When all phases are incompressible, compaction can only be accommodated through melt segregation. This is shown by the storage equation (2.13), which reduces to $\nabla \cdot \boldsymbol{q} = -\nabla \cdot \boldsymbol{v}_s$ when $\kappa_l \to \infty$ and $\kappa_s \to \infty$. When the mobility is small, viscous resistance in the melt is high, preventing melt from segregating quickly, and consequently the compaction rate is low. In this regime, $|\boldsymbol{q}| \propto M_\phi$ and Darcy dissipation increases with mobility (equation (2.39*c*)). As the mobility further increases, the melt's viscous stresses, which resist segregation and compaction, decrease. When the mobility is sufficiently large, compaction is no longer limited by viscous resistance to melt segregation, but instead by elastic resistance of the skeleton to isotropic stresses, controlled by the elastic compaction modulus κ_d. The critical mobility occurs when this elastic resistance prevents any further compaction of the solid. At this point, mass conservation forces the segregation flux to become constant (enforced by an increase in pore pressure gradient), while the heat producing viscous resistance to segregation decreases with $1/M_\phi$ (equation (2.39*c*)). Consequently, Darcy dissipation decreases with M_ϕ past this point.

(b) Influence of compressibility on tidal heating rates

In this section, we allow the solid and liquid phases to be compressible, while still imposing a constant melt fraction. We investigate the sensitivity of our tidal heating calculations to the bulk modulus of the liquid κ_l, as well as the compressibility of the two-phase aggregate (relative to the solid grains), by varying Biot's modulus α. We refer to a 'strong' asthenosphere as one with small α, and a 'weak' asthenosphere when α is large. Strong or weak in this context reflects the elastic resistance of the asthenosphere to compaction (isotropic) stresses, relative to a purely solid asthenosphere. The bulk modulus of the solid grains is held constant at $\kappa_s = 200\,\text{GPa}$.

We first determine the tidal dissipation sensitivity to compressible effects for shear heating in the poro-viscoelastic limit (§4b(i)). We then consider compaction heating while enforcing elastic shear (§4b(ii)). Finally, we investigate Darcy heating in the poroelastic limit (§4b(iii)).

(i) Shear heating

Here we consider the classic case of heating in the solid skeleton due to shear deformation, but for a partially molten medium. The results are shown in figure 2. We assume finite shear viscosity in the solid, η, infinite compaction viscosity, $\zeta \to \infty$ and fix the mobility to $M_\phi = 5 \times 10^{-7}\,\text{m}^2\,\text{Pa}^{-1}\,\text{s}^{-1}$. The liquid bulk modulus has minimal effect on shear heating, so we arbitrarily take $\kappa_l = 1\,\text{GPa}$. We also show solutions for a one-phase (solid-only) model ($\phi = \alpha = 0$).

The heating curves in figure 2a are minimally altered from the incompressible-phases case shown in figure 1a. Io-like heating rates are obtained on either side of the critical viscosity, for $\eta \sim$

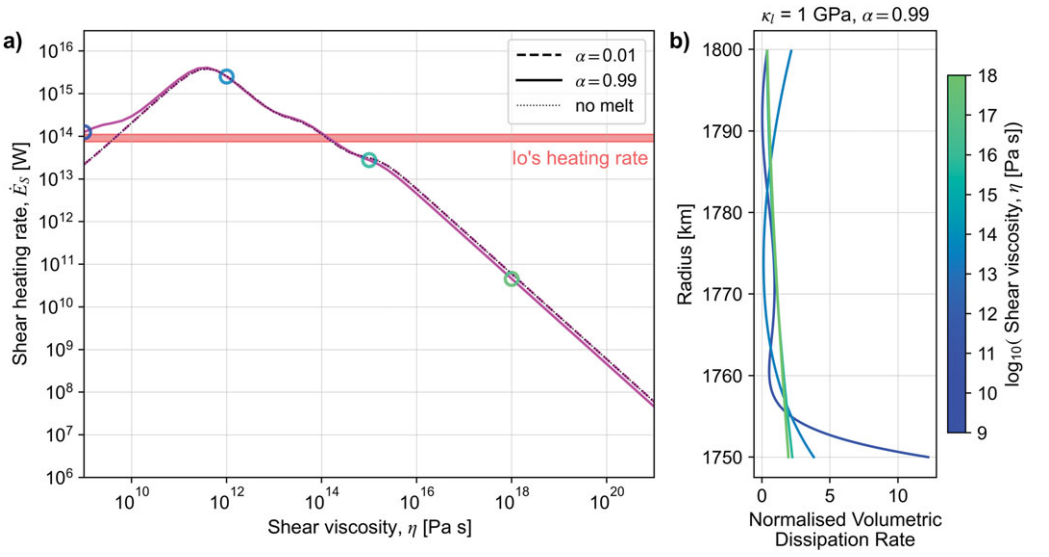

Figure 2. (a) Global- and time-averaged shear dissipation rate in the solid, $\dot{E}_S$, as a function of shear viscosity, η, for two different Biot's coefficient α. The black dotted line indicates the heating rate for a model with an entirely solid asthenosphere. (b) Normalized volumetric heating rate depth profiles for $\alpha = 0.99$ and $\kappa_l = 1$ GPa, which correspond to the open circles in panel (a). Normalization is taken relative to the mean heating rate. In both panels, the solid is taken to be elastic in shear ($\eta \to \infty$), ζ is taken to be independent of porosity (which is held at $\phi = 0.1$), the asthenosphere thickness is $H = 300$ km, and mobility is $M_\phi = 5 \times 10^{-7}$ m^2 Pa^{-1} s^{-1}.

10^{14} Pa s and 10^{10} Pa s. When the shear viscosity is ultra-low and sub-critical ($\eta \sim 10^9$ Pa s), melt enhances the shear-heating rate significantly when the asthenosphere is weaker to compaction ($\alpha = 0.99$). This enhanced heating rate is accompanied by a sharp increase in heating at the base of the asthenosphere, shown in figure 2b. However, for (more realistic) viscosities that exceed the critical value, melt plays a minor role in altering the shear heating rates.

(ii) Compaction heating

In the previous section, we suppressed compaction dissipation by taking $\zeta \to \infty$. Here, we relax this limit, and explore how compressibility of the melt and compactibility of the asthenosphere alters compaction heating. We force the solid to behave elastically under shear by taking $\eta \to \infty$, and fix the mobility to $M_\phi = 10^{-7}$ m^2 Pa^{-1} s^{-1}.

The total compaction dissipation rate is shown in figure 3a. The critical compaction viscosity at which compaction dissipation is maximized is sensitive to α but insensitive to κ_l. Smaller α (stronger matrix) pushes the critical compaction viscosity to larger ζ. The maximum possible compaction heating rate for this interior structure is approximately 1 TW (approx. 1% of Io's observed heating), occurring when $\zeta \sim 10^{15}$–10^{16} Pa s and $\alpha = 0.01$, which is broadly in agreement with [37] as discussed further in §5. Significantly smaller heating rates are obtained when the solid matrix is weak (compressible compared to the solid grains ($\alpha = 0.99$)). Although not shown, compaction heating rates that are 10% of Io's can be reached, but only when $M_\phi \gtrsim 10^{-3}$ m^2 Pa^{-1} s^{-1}. Below this value, compaction heating is insensitive to mobility.

Biot's coefficient controls the critical compaction viscosity because it alters the compaction Maxwell time of the asthenosphere. Maximum compaction dissipation occurs when the tidal forcing period is similar to the compaction Maxwell time, i.e. when $\omega\tau_C \sim 0.1$–1. The critical compaction viscosity is therefore $\zeta_{\text{crit}} \sim \kappa_d/\omega = (1-\alpha)\kappa_s/\omega$. Hence, when $\alpha \ll 1$, the critical compaction viscosity is dictated by the compressibility of only the solid grains. As the solid

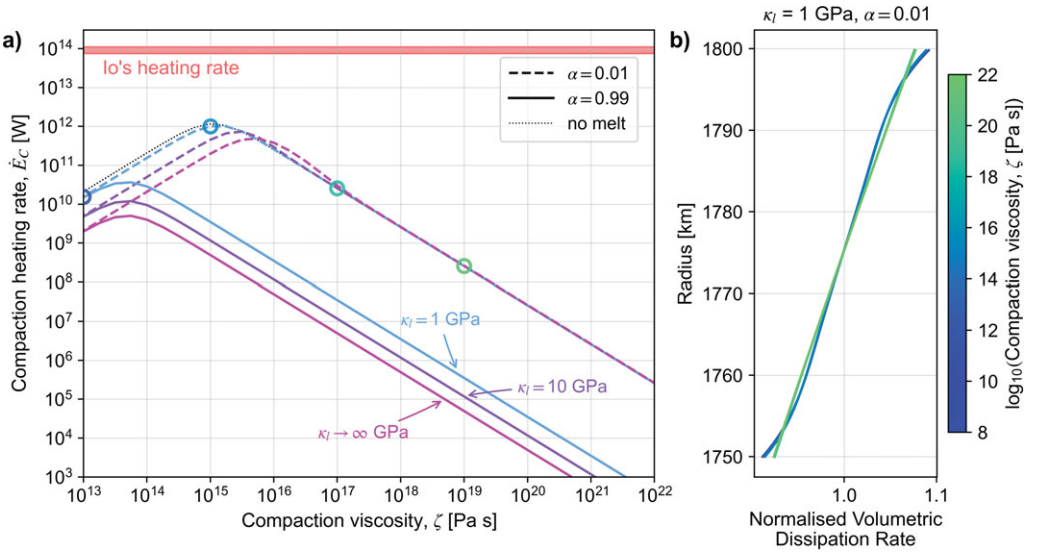

Figure 3. (a) Global- and time-averaged compaction dissipation rate in the solid, $\dot{E}_C$, as a function of compaction viscosity, ζ, for different liquid bulk moduli, κ_l, and Biot's coefficient α. (b) Normalized- and spherically averaged volumetric heating rate depth profiles for $\alpha = 0.01$ and $\kappa_l = 1$ GPa, which correspond to the open circles in panel (a). Normalization is taken relative to the mean heating rate. In both panels, the solid skeleton is taken to be elastic in shear ($\eta \to \infty$), ζ is taken to be independent of melt fraction (which is held at $\phi = 0.1$), the asthenosphere thickness is $H = 50$ km, and mobility is $M_\phi = 5 \times 10^{-7}$ m^2 Pa^{-1} s^{-1}.

grains become more incompressible, $\alpha \to 1$, so the critical compaction viscosity required to reach maximum heating decreases, which is the behaviour shown in figure 3a.

Figure 3 shows that the total compaction dissipation rate is dominantly controlled by compressibility of the solid skeleton relative to the solid grains. When the skeleton is strong against compaction (small α), higher heating rates can be achieved than when the skeleton is comparatively weak (large α). The compaction heating rate is partly controlled by $\mathrm{Im}(\tilde{\kappa}_d)$ equation (2.39*b*), as this dictates the viscous delay in response to compaction stresses. $\mathrm{Im}(\tilde{\kappa}_d)$ increases as the solid skeleton becomes increasingly strong ($\alpha \to 0$):

$$\mathrm{Im}(\tilde{\kappa}_d) = \frac{\omega\zeta}{1 + \frac{\omega^2\zeta^2}{(1-\alpha)^2\kappa_s^2}}. \tag{4.1}$$

The maximum value of $\mathrm{Im}(\kappa_d)$ occurs when $\alpha = 0$. This means that the viscous response to compaction is highest when the solid skeleton's elastic resistance to compaction is at its maximum, relative to the solid grains ($\kappa_d = \kappa_s$). Thus, somewhat counterintuitively, compaction dissipation is enhanced when the solid skeleton and solid grains have comparable compressibilities, rather than simply when the skeleton is easily compactible.

Figure 3a also shows that the total compaction heating rate generally increases as the melt becomes more compressible, provided that either α is large or the solid skeleton behaves viscously ($\zeta < \zeta_{\mathrm{crit}}$). This trend is controlled by how much the solid skeleton can (de)compact. If the melt is highly compressible, the solid skeleton can compact more before pore pressures become high enough to prevent further deformation. Compaction heating thus generally increases with more compressible melt. However, if the skeleton is both strong and behaves elastically under isotropic stresses ($\zeta > \zeta_{\mathrm{crit}}$), then the amount of compaction is no longer controlled by the pore pressure, and is instead controlled by the elastic resistance of the skeleton. In this case the melt's compressibility no longer controls the heating rate, which is why all dashed lines in figure 3a converge when the asthenosphere behaves elastically (large compaction viscosity).

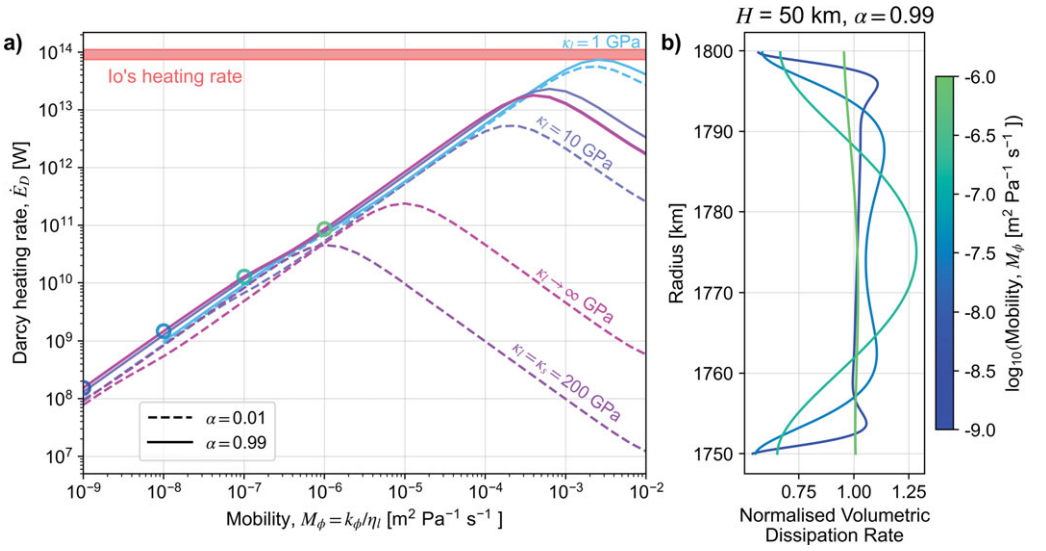

Figure 4. (a) Global- and time-averaged Darcy dissipation rate, $\dot{E}_D$, as a function of mobility, M_ϕ, for different liquid bulk moduli, κ_l, and Biot's coefficient α. The colours represent the bulk modulus (compressibility) of the melt, with warmer colours denoting a more incompressible melt. Note that the lower κ_l curves do not extend to the smallest mobilities due to numerical instability. (b) Normalized- and spherically averaged volumetric heating rate depth profiles, which correspond to the open circles in panel (a) for $\kappa_l \to \infty$. Normalization is taken relative to the mean heating rate. In both panels, the solid is taken to be elastic, M_ϕ is taken to be independent of melt fraction (which is held at $\phi = 0.1$), the asthenosphere is $H = 50$ km thick, and compaction dissipation is ignored.

In summary, compaction dissipation is maximized when (i) the skeleton is effective at resisting elastic compaction, $\alpha \ll 1$, and (ii) when ζ is close to its critical value so that $\omega\tau_C \sim 1$.

(iii) Darcy heating

The total Darcy dissipation rate $\dot{E}_D$ is given by integrating equation (2.39*c*) over the volume of the asthenosphere. The result is shown in figure 4a as a function of the melt mobility M_ϕ (equation (2.7)) for a moderately incompressible ($\alpha = 0.01$, dashed lines) and compressible ($\alpha = 0.99$, solid lines) poroelastic asthenosphere ($\eta \to \infty$, $\zeta \to \infty$).

We see that the critical mobility is sensitive to both κ_l and α. Maximum heating occurs at higher mobilities as the melt becomes more compressible and the skeleton becomes weaker to compaction. At mobilities less than critical, the Darcy dissipation rate is only weakly sensitive to α and melt compressibility, varying by a factor of approximately 2–3 between all cases shown. In contrast, α and κ_l strongly control the heating rate at mobilities greater than critical. The highest possible heating rate occurs for $\kappa_l = 1$ GPa when the mobility is approximately 3×10^{-3} m^2 Pa^{-1} s^{-1}, which can match Io's heat output. For a melt with $\eta_l = 1$ Pa s, this gives a permeability of $k = 3 \times 10^{-3}$ m^2. Such a high mobility (permeability) can only be attained if the effective grain size is larger than 10 cm (figure 5). This is discussed further in §5a.

As recognized in §4a for incompressible phases, the critical mobility occurs when elastic compaction becomes limited by elastic resistance of the skeleton, rather than the melt's viscous resistance to segregation. When this happens, the segregation flux becomes constant because Darcy flow is also limited by elastic resistance of the skeleton, rather than viscous resistance of the melt. When α is small, the skeleton has a greater resistance to elastic compaction, so melt segregation is limited at lower mobilities (i.e. at higher viscous resistance to Darcy flow). The critical mobility, as well as the maximum Darcy heating rate, therefore decreases with α. Liquid compressibility also affects the critical mobility. If the melt is compressible, then the segregation

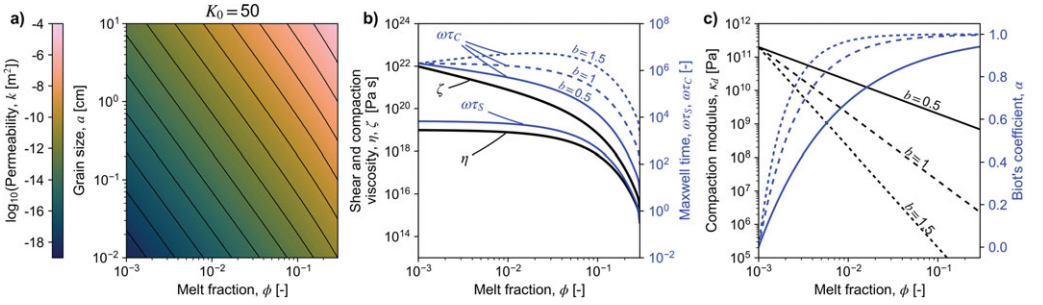

Figure 5. (a) Asthenosphere permeability as a function of melt fraction ϕ and grain size a, calculated using equation (4.2) with $K_0 = 50$. For the liquid viscosity of $\eta_l = 1$ Pa s used in the manuscript, the colour scale can equivalently be interpreted in terms of mobility $\log_{10}(M_\phi)$. (b) Compaction and shear viscosity (ζ and η, black), and the corresponding non-dimensional Maxwell times ($\omega\eta/\mu$ and $\omega\zeta/\kappa_d$, blue), as a function of melt fraction, calculated with equations (4.3) and (4.4). (c) Drained bulk modulus (black) and Biot's coefficient (blue) as a function of melt fraction, calculated with equations (4.7) and (4.8). The power-law exponent used to calculate κ_d in panels (b) and (c) is set to $b = 0.5$ (solid lines), 1 (long dashes), and 1.5 (short dashes).

flux can increase with mobility *past* the point at which compaction of the skeleton is limited by elasticity. The segregation flux is eventually limited when the melt can compress no further. Thus, for compressible melt, there is a decoupling between the mobility at which elastic compaction is halted, and the mobility at which melt segregation is limited. The critical mobility and maximum Darcy heating rate therefore generally increase as the melt becomes more compressible. This behaviour is the primary control on the Darcy heating rates shown in figure 4a.

In figure 4b, spherically averaged depth profiles of the volumetric Darcy dissipation rate are shown for a selection of mobilities and $\alpha = 0.99$. When the mobility is high (green line), Darcy dissipation is relatively uniform with radius across the asthenosphere. With decreasing mobility (green → blue lines), boundary layers emerge at the top and bottom of the asthenosphere. These boundary layers lead to numerical instability at small mobilities, as noted by RN22 and K23. The boundary-layer thickness scales with the compaction length of the asthenosphere, an emergent property of partially molten media [6,21].

(c) Total heating rate as a function of melt fraction

In the previous sections, rheological parameters were imposed independent of the melt fraction ϕ. In reality, the permeability of the interconnected pores, compaction/shear viscosity and drained bulk modulus all depend on ϕ. In this section we account for these dependencies, allowing us to gain a more physically consistent insight into how melt fraction controls Io's heating rate.

We assume that permeability scales with porosity as [6,57,58]

$$k(\phi) = \frac{a^2\phi^3}{K_0(1-\phi)^2}, \tag{4.2}$$

where a is the radius of the solid grains and $K_0 \approx 50$ is an empirically determined constant [59]. Figure 5a shows the permeability for different melt fractions and grain sizes using $K_0 = 50$. The highest permeability of $k = 10^{-5}$ m^2 occurs for the largest grain size of 10 cm at melt fractions of $\phi \sim 0.3$. For Earth-like mantle melt fractions of $\phi \sim 0.01$ and grain sizes of 1 mm, permeability is substantially smaller at $k \sim 10^{-12}$ m^2.

The compaction viscosity of Earth's mantle has never been directly measured [23]. Only [60] has experimentally inferred ζ from compaction rate experiments on peridotite samples. Yet its role is essential in a compacting poro-viscoelastic material. Assuming that compaction is associated with viscous deformation of grains during the closure/expansion of pores in partially molten

rock, it can be shown that the compaction viscosity should vary as [61,62]

$$\zeta(\phi) \approx \frac{\eta}{\phi}, \tag{4.3}$$

provided that the porosity is small. The compaction viscosity is therefore a property of the solid–liquid aggregate, rather than the solid grains. Also following [37,63], we modify the shear viscosity as a function of melt fraction through

$$\eta(\phi) = \eta_l \frac{1 + \Theta^\ell}{[1 - F(\Theta, \xi, \gamma)]^{5(1-\phi_*)/2}}, \tag{4.4}$$

where the additional auxiliary functions are

$$\Theta = \frac{1 - \phi}{1 - \phi_*} \tag{4.5}$$

and

$$F(\Theta, \xi, \gamma) = (1 - \xi)\mathrm{erf}\left(\frac{\sqrt{\pi}}{2(1-\xi)}\Theta(1 + \Theta^\gamma)\right). \tag{4.6}$$

The other rheological parameters are determined experimentally in [63], with $\ell = 25.7$, $\phi_* = 0.431$, $\xi = 1.17 \times 10^{-9}$ and $\gamma = 5$, which we take from table 3 in [37] (noting the typo in their ϕ_*, see [64]). The function in equation (4.4) accounts for the decrease of the shear viscosity due to grain-boundary lubrication by the melt. Hence, η is a property of the two-phase aggregate, and not a property of the solid grains.

Unlike [37], we keep μ constant. There is no experimental determination of how the elastic shear modulus should vary with melt fraction, but it is expected to be generally insensitive to ϕ except near the disaggregation limit [6]. Near disaggregation, it is questionable whether the rheological and two-phase model used here is valid. The bulk modulus of the solid grains κ_s is a property of the grains, not the two-phase aggregate, and so is independent of melt fraction.

Figure 5b plots equations (4.3) and (4.4) for ζ and η as a function of melt fraction. The shear viscosity stays roughly constant until $\phi \sim 0.05$, above which it decreases to about $\eta \sim 10^{15}$ Pa s at the disaggregation limit. The compaction viscosity decreases steadily as melt fraction increases, again until $\phi \sim 0.05$, at which point it rapidly decreases to $\zeta \approx 3\eta$ at the disaggregation limit. We also plot the Maxwell times for shear and compaction as a function of ϕ. For shear, $\omega\tau_S \sim 1$ very close to the disaggregation melt fraction. For compaction, $\omega\tau_C \sim 1$ again when close to disaggregation, but only for $b \lesssim 0.5$. Significant compaction dissipation is therefore favoured for small b.

Finally, the compaction modulus of the solid skeleton is also controlled by melt fraction [65]. The relationship between drained compaction modulus and melt fraction can be expressed in terms of another unknown rheological constant, the porosity bulk modulus (see eqn. 4.159 in [66]), which determines the skeleton's resistance to grain rearrangement. For simplicity, we instead adopt a power law relationship between κ_d and ϕ. As the melt fraction approaches zero, we expect that $\kappa_d \to \kappa_s$, because the solid skeleton adopts the properties of the grains themselves. We also expect κ_d to go to zero as $\phi \to \phi_{\mathrm{crit}}$, as there is then no coherent solid skeleton to resist isotropic stresses. This behaviour can be approximated by

$$\kappa_d(\phi) = \begin{cases} \kappa_s & \text{if } \phi < \phi_0, \\ \kappa_s \left(\frac{\phi_0}{\phi}\right)^b & \text{if } \phi_0 \le \phi < \phi_{\mathrm{crit}}, \\ 0 & \text{if } \phi \ge \phi_{\mathrm{crit}}, \end{cases} \tag{4.7}$$

where $b > 0$ is an unknown constant, and ϕ_0 is a small (but non-zero) melt fraction below which the skeleton behaves like a coherent solid, $\kappa_d = \kappa_s$. Correspondingly, Biot's coefficient becomes

$$\alpha(\phi) = \begin{cases} 0 & \text{if } \phi < \phi_0, \\ 1 - \left(\frac{\phi_0}{\phi}\right)^b & \text{if } \phi_0 \le \phi < \phi_{\text{crit}}, \\ 1 & \text{if } \phi \ge \phi_{\text{crit}}. \end{cases} \tag{4.8}$$

We adopt $\phi_0 = 10^{-3}$, and explore a range of b values. Both κ_d and α are shown as a function of melt fraction in figure 5c for $b = \{0.5, 1.0, 1.5\}$. Increasing melt fraction causes α to approach unity and κ_d to decrease. The increase in α and drop in κ_d is more rapid as b becomes larger. For $b \ll 1$, we always have $\alpha \ll 1$, even close to ϕ_{crit}. Thus, small b gives the asthenosphere a strong elastic resistance against compaction across the full range of relevant melt fractions, $0 < \phi < \phi_{\text{crit}}$.

The shear viscosity formulation in equation (4.4) is chosen to enable direct comparison with results from [37]. This formulation was developed to capture the increase in effective shear viscosity as interactions between suspended crystals begin to dominate the magma's rheology [63]. Alternative formulations are derived in terrestrial mantle deformation studies, where the microphysical mechanism that enables irreversible deformation gives rise to its own shear viscosity law. For instance, at sufficiently large grain sizes and/or high stress, dislocation creep is the dominant deformation mechanism [67]. However, at Io's high melt fraction, diffusion-accommodated grain-boundary sliding may instead be dominant [68]. Future work could explore the consequences of these different deformation mechanisms.

(i) Heating rates

In the following, we modify k, ζ, η, α and therefore κ_d, as functions of melt fraction using equations (4.2), (4.3), (4.4), (4.8) and (4.7), respectively. We take μ, κ_s and κ_l to all be independent of melt fraction.

Figure 6 shows the different contributions of Darcy, compaction, and shear dissipation to the total heating rate of our Io model. Darcy dissipation is substantially greater than shear dissipation across the middle range of melt fractions ($\phi \sim 0.05$–0.15), provided that the grain size is a greater than or approximately equal to 10 cm. For grain sizes that are less than 1 cm, it is at least two orders of magnitude less than the shear-heating rate at any melt fraction. The critical mobility is never encountered for any melt fraction. In all cases, the total dissipated power increases as the asthenosphere thickness is increased from $H = 50$ km (left) to 300 km (right), largely due to the increase in heat-producing volume.

Two-phase dynamics generally decreases both shear and compaction heating rates, as compared to the single-phase results. For shear heating, this decrease is minor. For compaction dissipation, figure 6 shows that this decrease is also minor, but this result is highly sensitive to the exponent b. As discussed with figure 3, there are two requirements to maximizing compaction dissipation: (i) the non-dimensional compaction Maxwell time of the asthenosphere must satisfy $\omega\tau_C \sim 0.1$–1 (i.e. ζ must be close to its critical value), and (ii) the solid matrix must be (relatively) elastically strong against compaction stresses, meaning α is small. The latter requirement can easily be satisfied in the one-phase model because $\alpha = 0$. To what degree these two requirements are met in the two-phase model depends on how sensitively α depends on melt fraction. Here, this sensitivity depends on the unknown exponent b through equation (4.8).

The relationship between Biot's coefficient and compaction dissipation as a function of b and ϕ is shown in figure 7. In panel (a) we see that the range of permitted α values (constrained by $\phi_0 < \phi < 0.3$) becomes increasingly small as b decreases. Hence, smaller b promotes an asthenosphere that can more effectively resist elastic compaction. Panel (b) shows that the maximum possible compaction dissipation rate is only reached as $b \to 0$, for any melt fraction. When $b = 1$, compaction dissipation peaks at small and large melt fractions, but is much weaker at intermediate melt fractions. When $b \lesssim 0.5$, compaction dissipation generally increases with melt fraction. Panel (c) shows how the compaction Maxwell time $\omega\tau_C$ varies with b, Biot's

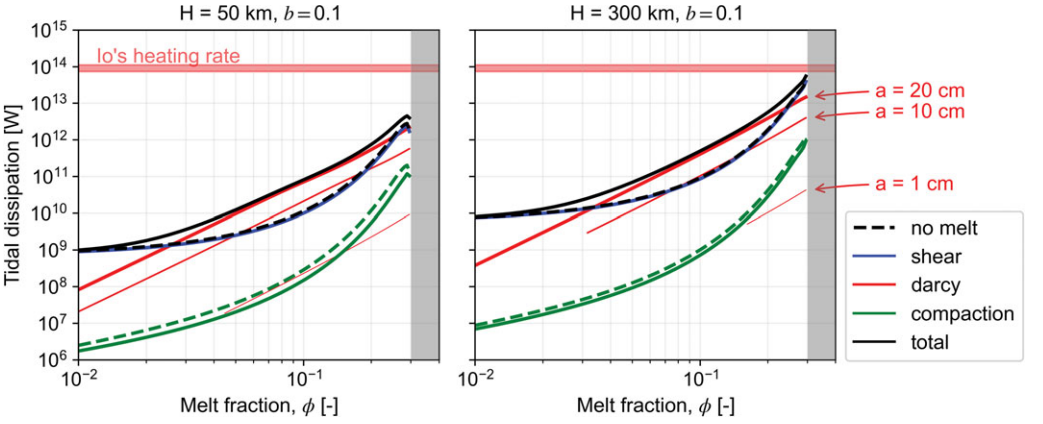

Figure 6. Tidal dissipation rate as a function of melt fraction for an asthenosphere thickness of $H = 50$ km (left) and 300 km (right). Solid lines are solutions computed for the two-phase problem, while dashed lines are solutions that neglect two-phase dynamics. The different colours represent dissipation from shear (blue), compaction (green), and Darcy (red) deformation. Compaction dissipation without melt (green dashed lines) is calculated for a single phase model where $\alpha = 0$ and $\phi = 0$, though ζ remains a function of ϕ, as in [37]. As labelled on the right, the different thickness of red line correspond to grain sizes of $a = 1$ cm (thin), 10 cm (medium), and 20 cm (thick). The black lines are the total dissipation for no melt (dashed) and largest grain size (solid). Curves do not extend across all melt fractions due to numerical instabilities encountered at small melt fractions/mobilities.

coefficient and melt fraction. We see that, as b decreases, $\omega\tau_C$ approaches unity at smaller α (stronger asthenosphere). Only for the largest melt fraction of $\phi = 0.3$ and smallest $b = 0.01$, does the asthenosphere reach $\omega\tau_C = 0.1$ and simultaneously have $\alpha \ll 1$. Thus, the two conditions to maximize compaction dissipation are more easily met for small b and high melt fraction. Physically, this means that for our self-consistent treatment of melt, the significance of compaction dissipation becomes a question of how quickly the solid skeleton becomes compactible (relative to the solid grains) after the onset of melting. When $b = 1$, α is very sensitive to melt fraction so the skeleton becomes rapidly compactible with increasing ϕ. In contrast, for $b = 0.01$, α is insensitive to ϕ, so the matrix remains highly uncompactible across the full range of possible melt fractions. This explains the main difference between our two-phase results and the single-phase results of [37], where they implicitly assume $\alpha = 0$. We discuss this point further in §5.

(d) Distribution of heating

A key observable property of Io is the distribution of volcanic activity at its surface. If the spatial dependence of tidal heat generation in its interior reflects the distribution of volcanic activity—a significant assumption—then volcanic activity provides a possible path to distinguishing between different tidal-heating modes. Hence, there is a history of comparing Io's volcanic distribution to patterns of tidal heat fluxes predicted by various models of tidal deformation and internal structures [35,69–71]. Imaging of Io by the Galileo and Juno spacecraft have now provided near-full coverage of the global distribution of hotspots. However, there is still active debate about the exact interpretation of this data. Ref. [72] finds that there is a greater concentration of hotspots towards the poles. Refs. [73] and [74] find that while there are, on average, the same areal density of volcanic hotspots across Io, those at lower latitudes have a greater thermal power emission. They argue that this is consistent with models considering solid-only heating in a shallow asthenopshere. Ref. [75] used a spherical harmonic decomposition of the hotspot distribution from 11 Juno flybys, finding that the activity is not strongly correlated to any of the solid-only or magma-ocean tidal heating models (e.g. [70]). Below, we compare the heating patterns predicted

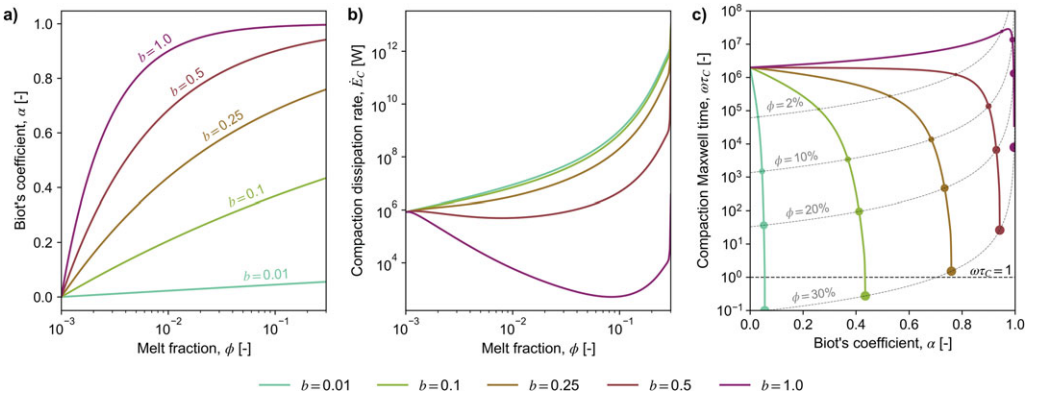

Figure 7. Effect of different b exponents on (a) Biot's coefficient and (b) compaction dissipation rate as a function of melt fraction, and (c) compaction Maxwell time $\omega\tau_C$ as a function of Biot's coefficient α. Also plotted in panel (c) are contours of melt fraction, and circles indicate where these intersect the Maxwell time curves for a given b. Panel (c) should thus be interpreted as representing the trajectory of α and $\omega\tau_C$ across the full range of melt fractions, for a given b. In this figure we have forced $k = 10^{-6}$ m^2 to aid numerical stability. The compaction dissipation rate is insensitive to k unless the mobility of the asthenosphere is greater than or approximately equal to 10^{-3} m^2 Pa^{-1} s^{-1}.

by the three deformation modes explored here, shear, compaction and Darcy deformation, shown in figure 8 for an $H = 300$ km thick asthenosphere.

All three heating patterns shown in figure 8 focus heating to low latitudes. Shear-generated heat flux is shown in panel (a), which shows a classic 'shallow' asthenosphere heating pattern [32], where heating is maximized at low latitudes, at the sub- and anti-Jovian longitudes ($\varphi = 0^\circ$ and 180°, respectively), and approximately $\pm 25^\circ$ above and below the equator. Our inclusion of two-phase flow does little to change this classic result. Compaction dissipation (panel (b)) has a heat flux of ~ 0.2 W m^{-2}, with maxima occurring either side of the sub- and anti-Jovian points, similar to that found by [37] (their figure 7). Regions of effectively zero heat flux occur north and south of these points. Darcy dissipation, shown in panel (c) for a high-mobility asthenosphere of $M_\phi = 10^{-5}$ m^2 Pa^{-1} s^{-1}, has dissipation maximized along the equator. The heat-flux magnitude is similar to that of compaction, and peaks at the sub- and anti-Jovian points. There is no longitudinal offset in peak heating, with minimum but non-zero heating at the poles. Overall, however, the broadest scales of heating are similar between compaction and Darcy dissipation.

Overall, our calculations suggest that all heating modes, if located in the asthenosphere, focus heating to low latitudes. Shear deformation causes the highest heating rates if Io's mantle's effective grain size cannot exceed 10 cm. Darcy dissipation heat fluxes can approach that due to shear deformation if the melt's mobility can approach $M_\phi \sim 10^{-3}$ m^2 Pa^{-1} s^{-1}. If tidal heating is directly correlated with the locations of surface volcanism on Io, then the inclusion of two-phase dynamics and physically consistent compaction dissipation does not change the general anticipation that shallow mantle tidal heating is focused towards low latitudes.

5. Discussion

We have shown with our two-phase mantle deformation model that melt segregation and viscous compaction of the two-phase assemblage can generate additional sources of heating in Io's interior. The exact proportion of Io's heating that is controlled by these mechanisms, relative to shear deformation, depends on the rheological properties of the asthenosphere. In §5a,b we discuss how these properties limit the upper bounds of Darcy and compaction dissipation. We identify the limitations and future avenues of this work in §5c.

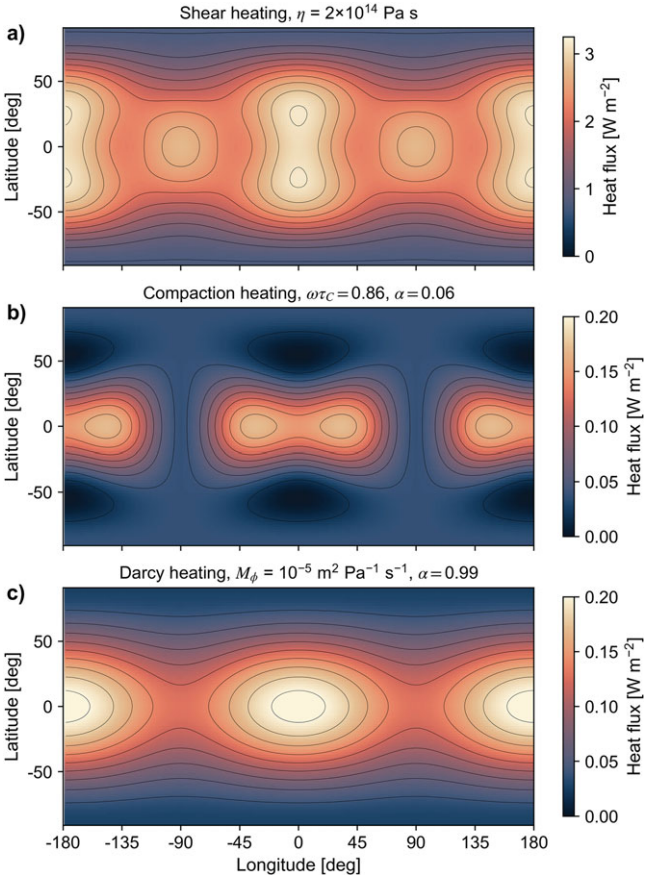

Figure 8. Surface heat flux patterns due to (a) shear, (b) compaction, and (c) Darcy deformation. These patterns are calculated with optimum parameters to maximize heating from each deformation mechanism. Darcy dissipation is calculated for a high mobility of 10^{-5} m^2 Pa^{-1} s^{-1}, corresponding to a grain size of $a \sim 10$ cm and melt fraction of $\phi \sim 0.3$ using equation (4.2). Compaction dissipation is calculated for optimum viscoelastic parameters at high melt fraction such that $\alpha \ll 1$ and $\zeta \sim 3.6 \times 10^{15}$ Pa s, and shear dissipation uses a low shear viscosity of $\eta = 2 \times 10^{14}$ Pa s.

(a) Magnitude of Darcy dissipation

The magnitude of Darcy dissipation is primarily controlled by the asthenosphere's mobility M_ϕ, the ratio of permeability k to melt viscosity η_l (equation (2.7)). As shown in figure 4, Io-like heating rates can be achieved for a high mobility of $M_\phi \sim 10^{-3}\,\mathrm{m^2\,Pa^{-1}\,s^{-1}}$. If the melt viscosity is $\eta_l = 1$ Pa s, then this requires a permeability of $k = 10^{-3}$ m^2. Our results in §4c set the permeability using the classic Kozeny–Carman relationship (equation (4.2)), and figure 5a shows that $k \sim 10^{-3}$ m^2 can only be achieved at grain sizes of $a > 10$ cm. If the Kozeny–Carman relationship is still valid at such large grain sizes, then the question becomes, what is the grain size in Io's mantle? Grain sizes in Earth's deep mantle are poorly known [76]. In the shallow mantle, observations and modelling suggest millimetre- to centimeter-sized grains [77,78]. Fluid alteration can potential yield grains sizes greater than 10 cm [76], though Io's interior is thought to be volatile depleted [79]. Modelling of Earth's Moon's tidal response suggests grain sizes of around 1 cm [80]. We therefore conclude that grain sizes in Io's mantle are unlikely to exceed approximately 10 cm.

Alternatively, we could interpret a high mobility as reflecting a large *effective* permeability (i.e. averaged over some large area or volume). This could arise from, for example, channelization

of magma within Io's asthenosphere. Magmatic channelization in Earth's asthenosphere is evidenced by tabular dunite zones found in ophiolites [81]. These channels are suspected to form via a reactive flow instability, where pressure-driven undersaturation in the magma forces a melting reaction, dissolving pyroxene and precipitating olivine from the melt onto the solid residuum [82,83]. The permeability of such channels would be orders of magnitude higher than the surrounding mantle, potentially large enough for turbulent dissipation. However, without observation of such structures on Io, this idea is only speculative.

If effective grain sizes of approximately 10 cm are possible, Darcy dissipation can exceed or match the shear-heating rate in the solid when the melt fraction is $0.05 < \phi < 0.2$, depending on the asthenosphere thickness and melt viscosity (figure 6). This conclusion hinges on the assumption that the asthenosphere behaves as a poro-viscoelastic *Maxwell* material, which we have used here. We know that in general, Maxwell viscoelastic models do not accurately predict attenuation rates that are measured from laboratory experiments across a range of frequencies [84,85]. The Andrade rheological model has been proposed as an alternative that better predicts attenuation in solid, cold, high-viscosity rock and ice [86]. However, while there are measurements of the attenuation behaviour of partially molten rock across seismic frequencies at small melt fractions ($\phi \sim 0.01$, [87]), there are, to our knowledge, no such measurements close to tidal frequencies and at large ($\phi \sim 0.1$) melt fractions. Moreover, Andrade model parameters have only been measured for shear deformation, while here we also consider isotropic deformation. It may be the case that an Andrade-type rheology is applicable to a partially molten asthenosphere, but it is not clear what the model's parameters should be when a high melt fraction, two-phase flow and compaction are included. This is not to say that an Andrade rheology is inappropriate to our case here, but merely that caution should be exercized when extending the model to additional deformation modes. We find, though, that two-phase flow dynamics has only a small effect on shear deformation of the solid skeleton. This small effect potentially indicates that, even with the caveats above, an Andrade model could still be an acceptable rheological description of shear deformation in a partially molten solid at high melt fraction.

It is also possible that Io's magma may be less viscous than the 1 Pa s assumed here. There is a general lack of evidence for chemically evolved, high-viscosity magmas on Io [8], with lava flow run-out distances and eruption temperatures consistent with low-viscosity, ultramafic melt [88,89]. Experimental determination of Earth-like upper-mantle basalt melts yield viscosities as low as approximately 0.1 Pa s [90]. Laboratory measurements of peridotite melt have determined that viscosities of even 0.01 Pa s are possible, though this requires slightly greater pressures than in the asthenosphere that we assume here [91]. Low viscosity melt enhances the liquid's mobility, generally increasing the Darcy dissipation rate. If the melt approached $\eta_l \sim 0.01$ Pa s in Io's hot asthenosphere, then Darcy dissipation could approach shear dissipation at a more moderate grain size of 1 cm. Note, though, that measurements of sulphur and chlorine isotopic anomalies in Io's tenuous atmosphere indicate a volatile-depleted interior [79]. Volatiles generally decrease the viscosity of magma, so these isotopic measurements could indicate that ultra-low magma viscosities are unlikely at the present day, depending on the magma's silica content.

Darcy (and compaction) heating, while smaller in magnitude than the global shear-heating rate, can still potentially be relevant in driving aspects of Io's internal dynamics at heating rates of 10^{11}–10^{12} W. This heating can be focused at different depths depending on the heating mechanism (figures 1–4), and hence the radial location of buoyancy sources may differ between Darcy, compaction and shear heating, potentially resulting in different mantle dynamics [41].

(b) Magnitude of compaction dissipation

Ref. [37] was the first to present tidal heating estimates for Io that included compaction dissipation. In their work, the asthenosphere was technically treated as a single-phase solid system. The viscoelastic parameters (η, ζ, κ_s, μ) all depended on melt fraction, but melt segregation (i.e. two-phase flow dynamics) was neglected. In particular, their $\kappa_s \to \kappa_l$ as $\phi \to \phi_{\text{crit}}$. In our two-phase approach, we have necessarily introduced the compaction modulus, κ_d, which

measures the (inverse) compressibility of the solid skeleton when the melt has been drained, rather than the grains themselves. This distinction is important; a two-phase aggregate with incompressible solid and liquid phases (κ_s, $\kappa_l \to \infty$) can itself be compressible at the macroscale (finite κ_d, $\alpha \to 1$), because the skeleton can rearrange grains while expelling/drawing in melt from its surroundings. This also means that κ_d can be less than κ_l.

We have shown that compaction dissipates heat most efficiently when $\kappa_d \sim \kappa_s$, such that $\alpha \ll 1$, and ζ is close to the critical value (figures 3 and 7). To our knowledge, only ζ has been inferred for Earth-like mantle material [23,60]. Biot's coefficient is indeed a function of melt fraction [65], as assumed in equation (4.8), but it is not clear whether α in Io's mantle should approach unity at the critical melt fraction ($b = 1$), or some small value ($b = 0.01$). If the former is true, meaning that the solid skeleton is easily (de)compacted when the melt fraction is high, then the possibility of significant compaction dissipation is precluded, as small enough α can never be achieved close to the critical compaction viscosity (figure 7c). How α actually depends on melt fraction is complex, and can be influenced by several factors including the pore geometry [65]. Given the role of Biot's coefficient in controlling compaction heating, the distinction between the single-phase approach of [37] and our two-phase approach can be critical.

If Io's melt is highly incompressible ($\kappa_l > 100\,\text{GPa}$), then high Darcy and compaction dissipation may be incompatible. We see this by comparing figures 3 and 4 for $\alpha = 0.01$ (dashed lines) and $\kappa_l = 200\,\text{GPa}$ (pink). When the mobility is high, $M_\phi = 10^{-3}\,\text{m}^2\,\text{Pa}^{-1}\,\text{s}^{-1}$, Darcy dissipation never exceeds 1 GW, while compaction can reach almost 1 TW at the critical viscosity. At these high mobilities, Darcy dissipation requires a weak asthenosphere to produce high heating rates, whereas compaction dissipation always requires a strong asthenosphere.

(c) Model limitations and future avenues

As shown in figure 8, tidal deformation naturally produces a spatially varying heat distribution. Hence, we expect melt generation to also vary in space, and consequently, melt fraction-dependent parameters such as permeability, shear and compaction viscosity, will too. However, the present formalism assumes that rheological parameters are laterally uniform and depend only on radius, as is typical in tidal deformation studies [46]. Sophisticated models of tidal deformation that take into account lateral variation in rheological parameters are emerging [92–94], though these do not yet take into account two-phase flow. While this is likely to change the exact spatial distribution of tidal heat generation, it is unlikely to change the overall picture of the importance of Darcy and compaction dissipation, relative to shear heating, in our results.

As with any tidal heating model, our results are generally sensitive to the rheological model assumed. We explore Io's two-phase tidal deformation under a compacting poro-viscoelastic Maxwell model, but, as discussed above, there may be better choices for a partially molten layer forced at tidal frequencies, such as the Andrade or Sunberg Cooper models [84,95]. We caution at choosing a more sophisticated rheology, however, because there is a lack of laboratory attenuation experiments that consider isotropic strain of the material. There is clearly a need to fill this gap if we are to understand the intricacies of Io's tidal heat generation.

Finally, a common assumption that is also made in this work is that the mantle melt fraction is constant in radius and does not vary over a deformation cycle. Neither of these points is likely to be true. Models of radial melt segregation that include a density contrast between solid and melt [28–30] all predict the formation of a compaction boundary layer, where the buoyant melt pools at the base of the lithosphere until it is extracted to the surface. This creates a highly non-uniform radial variation in melt fraction across the asthenosphere. Ref. [40] showed that additional Darcy dissipation may arise from these radial porosity gradients (see their eqn. (16)). However, as we have mentioned, their treatment of base-state porosity gradients is incomplete as ϕ is assumed constant in their (and our) storage equation (2.14). It is thus unclear whether radial porosity gradients will enhance or suppress Darcy and/or compaction dissipation. Given how extreme these gradients may become in a compacting boundary layer, this will be a topic of future work.

6. Conclusions

In this manuscript, we have combined viscoelastic tidal and poro-viscous compaction theories to develop a tidal deformation model that captures the two-phase dynamics of partially-molten planetary interiors. We derive the model, building upon the work of [39,40], using mathematically consistent constitutive laws that are inspired by the original work of A. E. Love [33]. The model can predict tidal heating from deformation due to shear, melt segregation/Darcy flow, and (de)compaction. We apply the model to the Jovian moon, Io, where we consider Io's asthenosphere to be partially molten with impermeable top and bottom boundaries. We investigate whether compaction and Darcy dissipation within the asthenosphere can contribute substantially to Io's total heat budget.

We find that Darcy dissipation is maximized when the asthenosphere is highly permeable, and the melt is low viscosity. To obtain Darcy heating rates that are comparable to shear heating requires a high enough permeability, which can only be achieved when the asthenosphere's grain size is at least 10 cm, the melt's viscosity is 1 Pa s, and the asthenosphere's melt fraction is between 5–20%. It is questionable whether such large grain sizes can be reached. If the melt is highly incompressible, then high Darcy dissipation additionally requires the asthenosphere to be weak to isotropic stresses. Compaction dissipation—heating due to the rearrangement of solid grains—is maximized when the asthenosphere is elastically resistant to isotropic stresses, when compared to the solid grains themselves. This means that high Darcy dissipation and high compaction dissipation may be incompatible, depending on the compressibility of the melt. While the heating patterns generated by Darcy and compaction dissipation are consistent with some interpretations of Io's distribution of volcanic hotspots, we find that compaction and Darcy dissipation are unlikely to account for more than approximately 1% of Io's observed total heat output if we assume realistic melt fractions, permeabilities and liquid viscosities. They may, however, still play a role in Io's convective dynamics. Future work on the evolution of grain size in tidally heated worlds would help further establish the role of Darcy dissipation in these types of planetary body.

These conclusions are reached by assuming that Io's asthenosphere behaves as a compacting poro-viscoelastic Maxwell material. While it is tempting to apply the more experimentally driven Andrade rheology to our model, the lack of laboratory measurements for partially molten rock under isotropic stresses make this approach unsatisfactory at present. We highlight the need for future experiments to measure the attenuation behaviour and poro-viscoelastic parameters of partially molten rock at (or near) tidal frequencies, with both shear and isotropic stresses.

By including viscous compaction of Io's two-phase asthenosphere, this study makes a first step at capturing the poro-viscoelastic dynamics of a partially molten tidally heated planetary body. This work thus moves us closer to self-consistently modelling the feedback associated with melt in Io's interior, and the inevitable viscous compaction of the mantle as a result. While we find it unlikely that Darcy dissipation can be a major contributor in Io's overall heat budget, melt segregation may still play a role in modulating eruption timing [15]. A future mission to Io would provide an invaluable means towards revealing the details of Io's melt distribution and dynamics [96].

Data accessibility. All figures are held in the Julia notebook repository [97].

The data are provided in the electronic supplementary material [98].

Declaration of AI use. We have not used AI-assisted technologies in creating this article.

Authors' contributions. H.C.F.C.H.: conceptualization, formal analysis, investigation, methodology, software, validation, visualization, writing—original draft, writing—review and editing; I.J.H.: conceptualization, funding acquisition, investigation, methodology, supervision, writing—review and editing; M.R.: investigation, writing—review and editing; R.F.K.: conceptualization, funding acquisition, investigation, methodology, project administration, supervision, writing—review and editing.

All authors gave final approval for publication and agreed to be held accountable for the work performed therein.

Conflict of interest declaration. We declare we have no competing interests.

Funding. This work was supported by a Leverhulme Trust Research Project grant no. (RPG-2021-199).
Acknowledgements. We are grateful to A. Veenstra for discussion and for pointing out a typo in [37] for the value of ϕ_*. For the purpose of open access, the author has applied a CC BY public copyright licence to any author accepted manuscript arising from this submission.

References

1. McEwen AS. 2002 Active Volcanism on Io. *Science* **297**, 2220–2221. (doi:10.1126/science.1076908)
2. Lainey V, Arlot JE, Karatekin Ö, Van Hoolst T. 2009 Strong tidal dissipation in Io and Jupiter from astrometric observations. *Nature* **459**, 957–959. (doi:10.1038/nature08108)
3. Williams JG, Boggs DH. 2015 Tides on the Moon: theory and determination of dissipation. *J. Geophys. Res.: Planets* **120**, 689–724. (doi:10.1002/2014JE004755)
4. Peale SJ, Cassen P, Reynolds RT. 1979 Melting of Io by tidal dissipation. *Science* **203**, 892–894. (doi:10.1126/science.203.4383.892)
5. Moore WB. 2001 The thermal state of Io. *Icarus* **154**, 548–550. (doi:10.1006/icar.2001.6739)
6. McKenzie D. 1984 The generation and compaction of partially molten rock. *J. Petrol.* **25**, 713–765. (doi:10.1093/petrology/25.3.713)
7. Morabito LA, Synnott SP, Kupferman PN, Collins SA. 1979 Discovery of currently active extraterrestrial volcanism. *Science* **204**, 972–972. (doi:10.1126/science.204.4396.972.a)
8. Keszthelyi L *et al.* 2001 Imaging of volcanic activity on Jupiter's Moon Io by Galileo during the Galileo Europa Mission and the Galileo Millennium Mission. *J. Geophys. Res.: Planets* **106**, 33025–33052. (doi:10.1029/2000JE001383)
9. Spencer JR *et al.* 2007 Io volcanism seen by New Horizons: a major eruption of the Tvashtar volcano. *Science* **318**, 240–243. (doi:10.1126/science.1147621)
10. Mura A *et al.* 2020 Infrared observations of Io from Juno. *Icarus* **341**, 113607. (doi:10.1016/j.icarus.2019.113607)
11. Witteborn FC, Bregman JD, Pollack JB. 1979 Io: an intense brightening near 5 micrometers. *Science* **203**, 643–646. (doi:10.1126/science.203.4381.643)
12. Veeder GJ, Matson DL, Johnson TV, Blaney DL, Goguen JD. 1994 Io's heat flow from infrared radiometry: 1983–1993. *J. Geophys. Res.: Planets* **99**, 17 095–17 162. (doi:10.1029/94JE00637)
13. Spencer JR, Sartoretti P, Ballester GE, McEwen AS, Clarke JT, McGrath MA. 1997 The Pele Plume (Io): observations with the Hubble Space Telescope. *Geophys. Res. Lett.* **24**, 2471–2474. (doi:10.1029/97GL02592)
14. Rathbun JA, Spencer JR. 2010 Ground-based observations of time variability in multiple active volcanoes on Io. *Icarus* **209**, 625–630. (doi:10.1016/j.icarus.2010.05.019)
15. de Kleer K, Nimmo F, Kite E. 2019 Variability in Io's volcanism on timescales of periodic orbital changes. *Geophys. Res. Lett.* **46**, 6327–6332. (doi:10.1029/2019GL082691)
16. de Pater I, Keane JT, de Kleer K, Davies AG. 2021 A 2020 Observational perspective of Io. *Annu. Rev. Earth Planet. Sci.* **49**, 643–678. (doi:10.1146/annurev-earth-082420-095244)
17. Khurana KK. 2011 Evidence of a global magma ocean in Io's interior. *Science* **332**, 1186–1189. (doi:10.1103/PhysRevA.85.033634)
18. Blöcker A, Saur J, Roth L, Strobel DF. 2018 MHD modeling of the plasma interaction with Io's asymmetric atmosphere. *J. Geophys. Res.: Space Phys.* **123**, 9286–9311. (doi:10.1029/2018JA025747)
19. Roth L, Saur J, Retherford KD, Blöcker A, Strobel DF, Feldman PD. 2017 Constraints on Io's interior from auroral spot oscillations. *J. Geophys. Res.: Space Phys.* **122**, 1903–1927. (doi:10.1002/2016JA023701)
20. Park RS *et al.* 2024 Io's tidal response precludes a shallow magma ocean. *Nature* **638**, 1–3. (doi:10.1038/s41586-024-08442-5)
21. Katz RF. 2022 *The dynamics of partially molten rock*. Princeton, NJ: Princeton University Press.
22. Spiegelman M. 1993 Physics of melt extraction: theory, implications and applications. *Phil. Trans. R. Soc. A* **342**, 23–41. (doi:10.1098/rsta.1993.0002)
23. Katz RF, Jones DWR, Rudge JF, Keller T. 2022 Physics of melt extraction from the mantle: Speed and style. *Annu. Rev. Earth Planet. Sci.* **50**, 507–540. (doi:10.1146/annurev-earth-032320-083704)
24. Fowler A. 1984 On the transport of moisture in polythermal glaciers. *Geophys. Astrophys. Fluid Dyn.* **28**, 99–140. (doi:10.1080/03091928408222846)

25. Schoof C, Hewitt I. 2016 A model for polythermal ice incorporating gravity-driven moisture transport. *J. Fluid Mech.* **797**, 504–535. (doi:10.1017/jfm.2016.251)
26. Haseloff M, Hewitt I, Katz R. 2019 Englacial pore water localizes shear in temperate ice stream margins. *J. Geophys. Res.: Earth Surface* **124**, 2521–2541. (doi:10.1029/2019JF005399)
27. Spencer DC, Katz RF, Hewitt IJ, May DA, Keszthelyi LP. 2020a Compositional layering in Io Driven by magmatic segregation and volcanism. *J. Geophys. Res.: Planets* **125**, e2020JE006604. (doi:10.1029/2020JE006604)
28. Spencer DC, Katz RF, Hewitt IJ. 2020b Magmatic intrusions control Io's crustal thickness. *J. Geophys. Res.: Planets* **125**, e2020JE006443. (doi:10.1029/2020JE006443)
29. Spencer DC, Katz RF, Hewitt IJ. 2021 Tidal controls on the lithospheric thickness and topography of Io from magmatic segregation and volcanism modelling. *Icarus* **359**, 114352. (doi:10.1016/j.icarus.2021.114352)
30. Miyazaki Y, Stevenson DJ. 2022 A subsurface magma ocean on Io: exploring the steady state of partially molten planetary bodies. *Planet. Sci. J.* **3**, 256. (doi:10.3847/PSJ/ac9cd1)
31. Steinke T, Hu H, Höning D, van der Wal W, Vermeersen B. 2020 Tidally induced lateral variations of Io's interior. *Icarus* **335**, 113299. (doi:10.1016/j.icarus.2019.05.001)
32. Segatz M, Spohn T, Ross MN, Schubert G. 1988 Tidal dissipation, surface heat flow, and figure of viscoelastic models of Io. *Icarus* **75**, 187–206. (doi:10.1016/0019-1035(88)90001-2)
33. Love AEH. 1911 *Some problems of geodynamics: being an essay to which the Adams Prize in the University of Cambridge was adjudged in 1911*. Cambridge, UK: Cambridge University Press.
34. Beuthe M. 2013 Spatial patterns of tidal heating. *Icarus* **223**, 308–329. (doi:10.1016/j.icarus.2012.11.020)
35. Bierson CJ, Nimmo F. 2016 A test for Io's magma ocean: modeling tidal dissipation with a partially Molten Mantle. *J. Geophys. Res.: Planets* **121**, 2211–2224. (doi:10.1002/2016JE005005)
36. Veenstra A, Rovira-Navarro M, Steinke T, Davies AG, van der Wal W. 2025 Lateral melt variations induce shift in Io's peak tidal heating. *Nat. Commun.* **16**, 6798. (doi:10.1038/s41467-025-62059-4)
37. Kervazo M, Tobie G, Choblet G, Dumoulin C, Běhounková M. 2021 Solid tides in Io's partially molten interior: contribution of bulk dissipation. *Astron. Astrophys.* **650**, A72. (doi:10.1051/0004-6361/202039433)
38. Liao Y, Nimmo F, Neufeld JA. 2020 Heat production and tidally driven fluid flow in the permeable core of Enceladus. *J. Geophys. Res.: Planets* **125**, e2019JE006209. (doi:10.1029/2019JE006209)
39. Rovira-Navarro M, Katz RF, Liao Y, van der Wal W, Nimmo F. 2022 The tides of Enceladus' porous core. *J. Geophys. Res.: Planets* **127**, e2021JE007117. (doi:10.1029/2021JE007117)
40. Kamata S. 2023 Poroviscoelastic gravitational dynamics. *J. Geophys. Res.: Planets* **128**, e2022JE007700. (doi:10.1029/2022JE007700)
41. Tackley PJ, Schubert G, Glatzmaier GA, Schenk P, Ratcliff JT, Matas JP. 2001 Three-dimensional simulations of Mantle Convection in Io. *Icarus* **149**, 79–93. (doi:10.1006/icar.2000.6536)
42. Yang XS. 2000 Nonlinear viscoelastic compaction in sedimentary basins. *Nonlinear Process. Geophys.* **7**, 1–8. (doi:10.5194/npg-7-1-2000)
43. Gassman F. 1951 Über Die elastizität Poröser medien. *Vierteljahrsschrift der Naturforschenden Gesellschaft in Zürich* **96**, 1–23.
44. Biot MA. 1956 Theory of propagation of Elastic Waves in a fluid-saturated porous solid. I. Low-frequency range. *J. Acoust. Soc. Am.* **28**, 168–178. (doi:10.1121/1.1908239)
45. Biot MA, Willis DG. 1957 The elastic coefficients of the theory of consolidation. *J. Appl. Mech.* **24**, 594–601. (doi:10.1115/1.4011606)
46. Sabadini R, Vermeersen B, Cambiotti G. 2016 *Global Dynamics of the Earth*. Springer. Dordrecht, The Netherlands.
47. Kaula WM. 1961 Analysis of gravitational and geometric aspects of geodetic utilization of satellites. *Geophys. J. Int.* **5**, 104–133. (doi:10.1111/j.1365-246X.1961.tb00417.x)
48. Hay HC, Trinh A, Matsuyama I. 2020 Powering the Galilean satellites with moon-moon tides. *Geophys. Res. Lett.* **47**, e2020GL088317. (doi:10.1029/2020GL088317)
49. Hay HC, Matsuyama I, Pappalardo RT. 2022 The high-frequency tidal response of ocean worlds: application to Europa and Ganymede. *J. Geophys. Res.: Planets* **127**, e2021JE007064. (doi:10.1029/2021JE007064)
50. Anderson JD, Sjogren WL, Schubert G. 1996 Galileo gravity results and the internal structure of Io. *Science* **272**, 709–712. (doi:10.1126/science.272.5262.709)

51. Anderson JD, Jacobson RA, Lau EL, Moore WB, Schubert G. 2001 Io's gravity field and interior structure. *J. Geophys. Res.: Planets* **106**, 32963–32969. (doi:10.1029/2000JE001367)
52. Aygün B, Čadek O. 2025 Love numbers for Io with a Magma Ocean. *Icarus* **436**, 116567. (doi:10.1016/j.icarus.2025.116567)
53. Schenk PM, Bulmer MH. 1998 Origin of mountains on Io by thrust faulting and large-scale mass movements. *Science* **279**, 1514–1517. (doi:10.1126/science.279.5356.1514)
54. Turtle EP *et al.* 2001 Mountains on Io: high-resolution Galileo observations, initial interpretations, and formation models. *J. Geophys. Res.: Planets* **106**, 33175–33199. (doi:10.1029/2000JE001354)
55. Davies AG. 2003 Volcanism on Io: estimation of eruption parameters from Galileo NIMS data. *J. Geophys. Res. E: Planets* **108**, 10–1. (doi:10.1029/2001je001509)
56. Hay HC, Hewitt I, Rovira-Navarro M, Katz RF. 2025 Julia notebook for poro-viscoelastic tidal heating of Io. Zenodo. (doi:10.5281/zenodo.15828786)
57. Dullien FA. 2012 *Porous media: fluid transport and pore structure*. New York (Orlando, FL/London/San Diego, CA): Academic press.
58. Rudge JF. 2018 Textural equilibrium melt geometries around tetrakaidecahedral grains. *Proc. R. Soc. A* **474**, 20170639. (doi:10.1098/rspa.2017.0639)
59. Bear J. 1972 Dynamics of fluid in porous media. New York, NY: Dover Publications, Elsevier.
60. Renner J, Viskupic K, Hirth G, Evans B. 2003 Melt extraction from partially molten peridotites. *Geochem. Geophys. Geosyst.* **4**, 2002GC000369. (doi:10.1029/2002GC000369)
61. Batchelor GK. 1967 *An introduction to fluid dynamics*. Cambridge, UK: Cambridge university press.
62. Hewitt I, Fowler A. 2008 Partial melting in an upwelling mantle column. *Proc. R. Soc. A* **464**, 2467–2491. (doi:10.1098/rspa.2008.0045)
63. Costa A, Caricchi L, Bagdassarov N. 2009 A model for the rheology of particle-bearing suspensions and partially molten rocks. *Geochem. Geophys. Geosyst.* **10**, 2008GC002138. (doi:10.1029/2008GC002138)
64. Kervazo M, Tobie G, Choblet G, Dumoulin C, Běhounková M. 2022 Inferring Io's interior from tidal monitoring. *Icarus* **373**, 114737. (doi:10.1016/j.icarus.2021.114737)
65. Selvadurai APS, Suvorov AP. 2020 The influence of the pore shape on the bulk modulus and the Biot coefficient of fluid-saturated porous rocks. *Sci. Rep.* **10**, 18959. (doi:10.1038/s41598-020-75979-6)
66. Cheng AHD. 2016 *Poroelasticity*. Theory and Applications of Transport in Porous Media. Cham, Switzerland: Springer International Publishing.
67. Kohlstedt DL, Goetze C. 1974 Low-stress high-temperature creep in olivine single crystals. *J. Geophys. Res. (1896–1977)* **79**, 2045–2051. (doi:10.1029/JB079i014p02045)
68. Hirth G, Kohlstedt DL. 1995 Experimental constraints on the dynamics of the partially molten upper Mantle: 2. Deformation in the dislocation creep regime. *J. Geophys. Res.: Solid Earth* **100**, 15 441–15 449. (doi:10.1029/95JB01292)
69. Rathbun JA, Lopes RM, Spencer JR. 2018 The global distribution of active Ionian volcanoes and implications for tidal heating models. *Astron. J.* **156**, 207. (doi:10.3847/1538-3881/aae370)
70. Matsuyama IN, Steinke T, Nimmo F. 2022 Tidal heating in Io. *Elements* **18**, 374–378. (doi:10.2138/gselements.18.6.374)
71. Aygün B, Čadek O. 2024 Tidal heating in a subsurface magma ocean on Io revisited. *Geophys. Res. Lett.* **51**, e2023GL107869. (doi:10.1029/2023GL107869)
72. Zambon F *et al.* 2023 Io hot spot distribution detected by Juno/JIRAM. *Geophys. Res. Lett.* **50**, e2022GL100597. (doi:10.1029/2022GL100597)
73. Davies AG, Perry JE, Williams DA, Nelson DM. 2024 Io's polar volcanic thermal emission indicative of magma ocean and shallow tidal heating models. *Nature Astron.* **8**, 94–100. (doi:10.1038/s41550-023-02123-5)
74. Davies AG, Perry JE, Williams DA, Veeder GJ, Nelson DM. 2024 New global map of Io's volcanic thermal emission and discovery of hemispherical dichotomies. *Planet. Sci. J.* **5**, 121. (doi:10.3847/PSJ/ad4346)
75. Pettine M, Imbeah S, Rathbun J, Hayes A, Lopes RMC, Mura A, Tosi F, Zambon F, Bertolino S. 2024 JIRAM observations of volcanic flux on Io: distribution and comparison to tidal heat flow models. *Geophys. Res. Lett.* **51**, e2023GL105782. (doi:10.1029/2023GL105782)
76. Dannberg J, Eilon Z, Faul U, Gassmöller R, Moulik P, Myhill R. 2017 The importance of grain size to Mantle dynamics and seismological observations. *Geochem. Geophys. Geosyst.* **18**, 3034–3061. (doi:10.1002/2017GC006944)

77. Hirth G, Kohlstedt D. 2003 Rheology of the upper Mantle and the Mantle wedge: a view from the experimentalists. In *Geophysical Monograph Series*, pp. 83–105. American Geophysical Union. (doi:10.1029/138GM06)
78. Ruh JB, Tokle L, Behr WM. 2022 Grain-size-evolution controls on lithospheric weakening during continental rifting. *Nat. Geosci.* **15**, 585–590. (doi:10.1038/s41561-022-00964-9)
79. de Kleer K, Hughes EC, Nimmo F, Eiler J, Hofmann AE, Luszcz-Cook S, Mandt K. 2024 Isotopic evidence of long-lived volcanism on Io. *Science* **384**, 682–687. (doi:10.1126/science.adj0625)
80. Nimmo F, Faul UH, Garnero EJ. 2012 Dissipation at tidal and seismic frequencies in a melt-free Moon. *J. Geophys. Res.: Planets* **117**, 2012JE004160. (doi:10.1029/2012JE004160)
81. Quick JE. 1982 The origin and significance of large, tabular dunite bodies in the trinity peridotite, Northern California. *Contrib. Mineral. Petrol.* **78**, 413–422. (doi:10.1007/BF00375203)
82. Aharonov E, Whitehead JA, Kelemen PB, Spiegelman M. 1995 Channeling instability of upwelling melt in the Mantle. *J. Geophys. Res.: Solid Earth* **100**, 20 433–20 450. (doi:10.1029/95JB01307)
83. Rees Jones DW, Katz RF. 2018 Reaction-infiltration instability in a compacting porous medium. *J. Fluid Mech.* **852**, 5–36. (doi:10.1017/jfm.2018.524)
84. McCarthy C, Cooper RF. 2016 Tidal dissipation in creeping ice and the thermal evolution of Europa. *Earth Planet. Sci. Lett.* **443**, 185–194. (doi:10.1016/j.epsl.2016.03.006)
85. Bierson CJ. 2024 The impact of rheology model choices on tidal heating studies. *Icarus* **414**, 116026. (doi:10.1016/j.icarus.2024.116026)
86. Castillo-Rogez JC, Efroimsky M, Lainey V. 2011 The tidal history of Iapetus: Spin dynamics in the light of a refined dissipation model. *J. Geophys. Res.: E: Planets* **116**, 1–29. (doi:10.1029/2010JE003664)
87. Jackson I, Faul UH, Fitz Gerald JD, Tan BH. 2004 Shear wave attenuation and dispersion in melt-bearing olivine polycrystals: 1. Specimen fabrication and mechanical testing. *JGR: Solid Earth* **109**, 2003JB002406. (doi:10.1029/2003JB002406)
88. McEwen AS *et al.* 1998 High-temperature silicate volcanism on Jupiter's Moon Io. *Science* **281**, 87–90. (doi:10.1126/science.281.5373.87)
89. Keszthelyi L, Jaeger W, Milazzo M, Radebaugh J, Davies AG, Mitchell KL. 2007 New estimates for Io eruption temperatures: implications for the interior. *Icarus* **192**, 491–502. (doi:10.1016/j.icarus.2007.07.008)
90. Kushiro I. 1986 Viscosity of partial melts in the upper Mantle. *JGR* **91**, 9343. (doi:10.1029/JB091iB09p09343)
91. Liebske C, Schmickler B, Terasaki H, Poe BT, Suzuki A, Funakoshi K, Ando R, Rubie DC. 2005 Viscosity of peridotite liquid up to 13 GPa: implications for magma ocean viscosities. *Earth Planet. Sci. Lett.* **240**, 589–604. (doi:10.1016/j.epsl.2005.10.004)
92. Beuthe M. 2019 Enceladus's crust as a non-uniform thin shell: II tidal dissipation. *Icarus* **332**, 66–91. (doi:10.1016/j.icarus.2019.05.035)
93. Rovira-Navarro M, Matsuyama I, Berne A. 2024 A spectral method to compute the tides of laterally heterogeneous bodies. *Planet. Sci. J.* **5**, 129. (doi:10.3847/PSJ/ad381f)
94. Berne A, Simons M, Keane JT, Park RS. 2023 Inferring the mean thickness of the outer ice shell of enceladus from diurnal crustal deformation. *J. Geophys. Res.: Planets* **128**, e2022JE007712. (doi:10.1029/2022JE007712)
95. Renaud JP, Henning WG. 2017 Increased tidal dissipation using advanced rheological models: implications for Io and tidally active exoplanets. *Astrophys. J.* **857**, 98. (doi:10.3847/1538-4357/aab784)
96. Keane J *et al.* 2021 The science case for Io exploration. *Bull. Am. Astron. Soc.* **53**, 178. (doi:10.3847/25c2cfeb.f844ca0e)
97. Hay H. 2025 Julia Notebook for "Poro-viscoelastic Tidal Heating of Io". Zenodo. (doi:10.5281/zenodo.17048152)
98. Hay HCFC, Hewitt I, Rovira-Navarro M, Katz RF. 2025 Poro-viscoelastic tidal heating of Io. Figshare. (doi:10.6084/m9.figshare.c.8061268)